Soil Dynamics and Earthquake Engineering 211 (2026) 110619

Contents lists available at ScienceDirect

Soil Dynamics and Earthquake Engineering

journal homepage: www.elsevier.com/locate/soildyn

A probabilistic framework for post-earthquake safety assessment of mainshock-damaged buildings

Saeed Amiri, Sanda Koboevic *

Department of Civil, Geological and Mining Engineering, Polytechnique Montréal, Montréal, QC, Canada

ARTICLE INFO

Keywords:
Collapse safety index
Post-earthquake probabilistic assessment
Mainshock-aftershock sequences
Collapse capacity
Reoccupation assessment
Incremental dynamic analysis
Engineering demand parameters

ABSTRACT

Evaluating the safety of buildings for reoccupation after a mainshock, while accounting for possible aftershocks, remains a major challenge in post-earthquake decision-making. Conventional tagging methods rely on deterministic safety thresholds that assume fixed residual collapse capacity and neglect the variability inherent in nonlinear structural response. In addition, the selection of such safety thresholds is often subjective and based on expert judgment, while decisions are typically derived from a single deformation-based damage measure. This study introduces a probabilistic framework for post-mainshock safety evaluation that addresses these limitations by explicitly quantifying uncertainty and incorporating multiple engineering demand parameters (*EDPs*), including maximum drift, residual drift, and the Park-Ang damage index. The reduction in collapse capacity is obtained from sequential incremental dynamic analyses, and the probability that a damaged building becomes unsafe under aftershocks is estimated from statistically fitted *EDP* distributions with bootstrap-based uncertainty quantification. Application to a four-story steel moment-resisting frame demonstrates the implementation of the proposed methodology and shows its ability to provide an objective probabilistic basis for safety classification and post-earthquake reoccupation assessments.

1. Introduction

Assessing the safety of buildings damaged by a mainshock is critical in the post-earthquake environment. Traditionally, decisions about reoccupation have relied on visual inspections and qualitative guidelines developed from past earthquake experiences [1,2]. These methods are inherently subjective, often influenced by engineers' interpretations, and focused primarily on the mainshock's effects. Ideally, such an assessment should be conducted by structural engineering specialists. However, after a major earthquake, the shortage of qualified professionals often forces urgent decisions to be made by engineers with varying levels of experience. Even experienced professionals struggle to agree on damage severity because qualitative categories such as slight, moderate, or extensive remain open to interpretation [3]. This results in significant uncertainty in post-mainshock evaluations and highlights the need for more objective, standardized frameworks that can be applied efficiently across a wide range of buildings and scenarios.

The challenge is further amplified by the short time interval that may separate the mainshock from damaging aftershocks. For instance, in the 2011 Tohoku earthquake and the 2004 Sumatra-Andaman earthquake, strong aftershocks occurred within hours of the main event [4,5]. These time-critical conditions necessitate rapid and reliable damage assessments to determine the safety and serviceability of structures prior to the arrival of strong aftershocks [6–8]. In these high-pressure scenarios, simulation-based methodologies can offer critical support, enabling timely evaluations when on-site inspections are impractical. Developing these tools into user-friendly digital platforms could significantly help inspectors make quick, informed decisions in the field.

In recent decades, several devastating seismic sequences have demonstrated the need to explicitly account for aftershocks in safety assessments. For example, the 2010-2011 Canterbury earthquake sequence in New Zealand involved several strong and damaging events, some of which occurred within a short period and resulted in widespread damage and 185 fatalities. The 2011 Tohoku earthquake in Japan, followed by hundreds of strong aftershocks and a tsunami, destroyed over 128,000 houses and claimed nearly 16,000 lives [9]. Similarly, the 2015 Gorkha earthquake in Nepal and the 2023 Turkey-Syria earthquakes caused catastrophic damage and thousands of fatalities within hours or days of the mainshock [10,11]. These events underscore the urgent need for evaluation frameworks that explicitly

* Corresponding author.
E-mail address: sanda.koboevic@polymtl.ca (S. Koboevic).

https://doi.org/10.1016/j.soildyn.2026.110619
Received 4 May 2026; Received in revised form 29 July 2026; Accepted 31 July 2026
Available online 13 August 2026
0267-7261/© 2026 The Authors. Published by Elsevier Ltd. This is an open access article under the CC BY-NC license (http://creativecommons.org/licenses/by-nc/4.0/).

account for the combined effects of mainshock–aftershock sequences. Recent studies following the 2023 Kahramanmaraş earthquake sequence in Türkiye, such as [12,13], have further emphasized the challenges associated with assessing building safety after successive strong ground motions. However, most seismic codes still focus on single-event scenarios [14,15], leaving a critical gap in post-earthquake safety decision-making.

ATC-20 [16] introduced guidelines to facilitate rapid visual inspections after earthquakes, involving green, yellow, and red tags to indicate occupancy safety. FEMA P-58 [17] extends this concept by providing a probabilistic assessment of whether structural or non-structural damage warrants an unsafe placard. However, neither method directly quantifies the residual structural safety of earthquake-damaged buildings subjected to aftershocks.

In response to these limitations, several studies have explored analytical and simulation-based methods to improve post-earthquake safety assessments. Bazzurro et al. [18] developed a methodology to support post-earthquake building tagging by linking pre-earthquake nonlinear analyses with expected aftershock demands, enabling a probabilistic assessment of residual capacity and occupancy safety. Luco et al. [19] assessed residual capacity using both static and dynamic methods. Ruiz-García and Aguilar [20] introduced a residual capacity index to quantify collapse capacity following mainshock-induced residual drift, highlighting the role of aftershock polarity. Burton and Sharma [21] applied Incremental Dynamic Analysis (IDA) [22] to mainshock-damaged RC frames, while Burton et al. [23] introduced safety indices incorporating residual capacity and collapse probability. Zhang et al. [24] employed machine learning to map damage patterns to safety classifications. Kalateh-Ahani and Amiri [25] used the Park-Ang index [26] and back-to-back IDAs to assess collapse capacity, and Galvis et al. [27] examined damage indicators and their robustness under model uncertainty.

Despite recent advances in post-earthquake safety assessment, most existing approaches rely on median collapse capacities and assume abrupt strength loss, thereby overlooking the variability and associated uncertainties in structural response. Such simplifications are often inadequate for quantifying realistic safety margins in the post-mainshock environment, where both record-to-record variability and residual damage effects play critical roles. Moreover, existing approaches rarely provide a consistent basis for linking observable engineering demand parameters, such as peak drift, residual drift, or cumulative damage, to explicit probabilistic safety metrics, leaving inspectors without a clear tool for translating observed post-mainshock damage into rational reoccupation decisions. While several studies have addressed aspects of post-earthquake safety assessment, they do not typically simultaneously integrate deformation-, residual-, and energy-based EDPs within a probabilistic formulation, nor consistently link observed damage to safety metrics across a spectrum of residual-capacity thresholds.

To address these gaps, this study proposes a probabilistic framework that explicitly accounts for uncertainty and directly links measured structural damage to quantifiable safety indices. Building on prior work, the framework integrates multiple deformation- and energy-based *EDPs* within a statistically calibrated formulation, providing a consistent basis for post-mainshock safety evaluation. Collapse safety index (κ) is introduced as the ratio of the collapse-level intensity measure of the damaged structure to that of the intact one, representing the reduction in residual collapse capacity due to mainshock damage. Sequential Incremental Dynamic Analyses (IDAs) are performed for both intact and damaged configurations under recorded aftershocks, using multiple engineering demand parameters (*EDPs*), including maximum drift, residual drift, and the Park-Ang damage index. Statistical distributions are then fitted to the *EDPs* associated with different κ thresholds to estimate the probability that a damaged building becomes unsafe under aftershocks. The framework is demonstrated on a four-story steel moment-resisting frame subjected to 33 recorded mainshock-aftershock sequences, considering both peak- and cumulative-based *EDPs* and the effects of aftershock polarity. Results demonstrate how probabilistic metrics and the evaluation of candidate safety thresholds can enhance the consistency and reliability of post-earthquake reoccupation decisions.

The proposed methodology provides a structured basis for incorporating record-to-record variability, multiple damage indicators, and probabilistic safety thresholds into post-mainshock assessment. Its implementation requires greater analytical effort than rapid visual inspection methods because it relies on sequential nonlinear dynamic analyses, statistical distribution fitting, and multi-EDP calibration. The resulting probabilistic assessment is intended to complement, rather than replace, field inspection procedures by providing a more objective and uncertainty-informed basis for post-earthquake safety evaluation. Pre-computed analyses and future digital implementation reduce the associated computational demands and facilitate practical application within realistic post-earthquake decision-making time constraints. The following sections present the formulation of the collapse safety index, the derivation of EDP-based thresholds, the statistical modeling procedures and the application to the case-study building.

2. Methodology

2.1. Definitions and background

2.1.1. Collapse safety index

The collapse safety index κ is defined in Eq. (1) as the ratio of the median intensity measure (IM) at collapse of a mainshock-damaged structure to that of the intact structure [20,21,23–25,27].

$$\kappa = \frac{IM^{\mathrm{AS}}_{\mathrm{DMG,COL}}}{IM^{\mathrm{AS}}_{\mathrm{INT,COL}}} \tag{1}$$

In this equation, $IM^{\mathrm{AS}}_{\mathrm{DMG,COL}}$ denotes the intensity measure at which a building that has already sustained a certain level of damage from the mainshock reaches collapse under the excitation of the aftershock. $IM^{\mathrm{AS}}_{\mathrm{INT,COL}}$ represents the corresponding collapse intensity measure for the same structure in its intact (undamaged) state under the same aftershock excitation. These values are obtained through incremental dynamic analyses (IDAs) performed on predefined post-mainshock damage states and the undamaged configuration. Although the spectral acceleration at the fundamental period of the structure, $Sa(T_1)$, is a widely used ground-motion intensity measure, several studies have shown that the average spectral acceleration, $Sa_{avg}(T)$, is more effective in predicting nonlinear collapse [28–31]. Accordingly, this study adopts the $Sa_{avg}(T)$ formulation proposed in Ref. [31], as defined in Eq. (2).

$$Sa_{avg}(c_1T_1, \ldots, c_NT_1) = \left(\prod_{i=1}^{N} Sa(c_iT_1) \right)^{1/N} \tag{2}$$

Here, T_1 is the fundamental period of the structure, $Sa(c_iT_1)$ is the spectral acceleration at a period of c_iT_1, considering the 5% damping ratio, and N is the number of periods used to compute Sa_{avg}, over the range from 0.2 T_1 to 3.0 T_1 in increments of 0.01 s. Consequently, N depends on the fundamental period T_1 and, for the adopted period increment of 0.01 s, is given by $N = (3.0\ T_1 - 0.2\ T_1)/(0.01\mathrm{s}) + 1$. For the case study building with $T_1 = 1.55$ s, this gives $N = (4.65\text{-}0.31)/0.01 + 1 = 435$. It is worth noting that other IMs may also be incorporated into the proposed framework, provided that their efficiency and sufficiency are validated under sequential earthquakes.

2.1.2. Engineering demand parameters (EDPs)

Collapse is assumed to occur when an *EDP* reaches or exceeds its threshold. This study considers three *EDPs*: Peak Inter-story Drift Ratio (*PIDR*), Residual Inter-story Drift Ratio (*RIDR*), and the Park–Ang Damage Index (*DI*) [26]. *PIDR* is commonly used in seismic design and

assessment. *RIDR* captures permanent deformations and serves as a proxy for residual capacity and post-earthquake reparability, while *DI* quantifies cumulative damage by combining deformation and energy dissipation demands and is calculated using Eqs. (3)–(7) [26].

$$DI_k = \frac{\theta_m}{\theta_u} + \frac{\beta}{M_y\,\theta_u}\int dE \tag{3}$$

$$DI_{\text{story}} = \sum (\lambda_k)_{\text{component}}\,(DI_k)_{\text{component}} \tag{4}$$

$$(\lambda_k)_{\text{component}} = \left(\frac{E_k}{\sum E_k}\right)_{\text{component}} \tag{5}$$

$$(\lambda_j)_{\text{story}} = \left(\frac{E_j}{\sum E_j}\right)_{\text{story}} \tag{6}$$

$$DI = \sum (\lambda_j)_{\text{story}}\,(DI_j)_{\text{story}} \tag{7}$$

In these equations, θ_m denotes the maximum rotation of the section, θ_u is the ultimate rotation capacity of the section, $\int dE$ is the absorbed hysteretic energy of the section, M_y represents the yield moment, and β is a calibration factor accounting for the effect of the dissipated energy on structural damage. In this study β is set to 0.15, as recommended in Ref. [32]. E_k and E_j represent the total absorbed energy in the kth component and the jth story, respectively. $(\lambda_k)_{\text{component}}$ and $(\lambda_j)_{\text{story}}$ are the energy weighting factors. Story-level and global damage indices can be derived from the calculated component-level damage indices.

To evaluate how mainshock-induced structural damage affects κ, eight discrete limit states LS_1 - LS_8 are defined for each *EDP* (Table 1), with LS_8 corresponding to collapse. The principal thresholds are based on established guidelines for steel special moment frame (SMF) buildings. These include ASCE/SEI provisions for *PIDR* [33] (widely applied in the literature, e.g., Ref. [34]), FEMA P-58-1 recommendations for *RIDR* (frequently adopted in related studies, e.g., Ref. [17]), and Park and Ang damage index limits [26], which are broadly used to characterize generalized structural damage (e.g., Refs. [25,35]). Intermediate thresholds are introduced between these reference values to provide a finer discretization of the κ–EDP relationships used in the subsequent probabilistic analyses. These intermediate values are analytical subdivisions rather than additional code-defined performance limits. Because the adopted values represent generalized SMF performance objectives rather than building-specific capacities, they are considered appropriate for the 4-story case study. They may also be applied to other SMF buildings when a generalized performance classification is desired. However, different lateral-force-resisting systems, such as concentrically braced frames, eccentrically braced frames, or reinforced concrete moment-resisting frames, may require alternative threshold definitions reflecting their governing performance criteria and damage characteristics. Accordingly, the thresholds adopted herein should be viewed as system-specific assumptions for SMF buildings rather than universally applicable performance limits.

2.1.3. Existing operational rule

In conventional post-earthquake safety assessments, the residual collapse capacity of a damaged building is expressed through the collapse-safety index κ. The safety for reoccupation is then evaluated deterministically by comparing the median κ with a prescribed minimum threshold $\kappa_{\min}$, which represents the minimum acceptable residual collapse capacity [20,21,24,25,27]. This threshold delineates the boundary between acceptable and unacceptable post-mainshock conditions, as originally proposed in prior studies [20,21,24,25,27]. The decision logic follows a simple binary rule: If $\kappa > \kappa_{\min}$, the building is considered "safe" for reoccupation; otherwise, it is "unsafe". In practice, $\kappa_{\min}$ is typically selected based on engineering judgment, with limited guidance on how different choices of this threshold affect the risk of aftershock-induced collapse.

While this deterministic tagging rule provides an intuitive basis for rapid post-event decisions, it has two key limitations. First, it neglects uncertainty: the conventional approach treats both the computed κ value and the threshold $\kappa_{\min}$ as deterministic quantities, overlooking the substantial record-to-record variability in collapse capacity revealed by nonlinear dynamic analysis. As a result, the method may misrepresent structural safety, particularly for buildings with κ values near the threshold, where the uncertainty plays a dominant role. Second, the decision is based on a single deformation-based indicator, most commonly peak inter-story drift, even though post-mainshock behavior depends on multiple aspects of structural response, including deformation, residual displacement, and cumulative damage. Measures such as *PIDR*, *RIDR*, and the *DI* capture different damage mechanisms and can provide complementary insight.

These limitations motivate the development of a probabilistic framework that (i) quantifies uncertainty in the reduction of collapse capacity after a mainshock, (ii) provides simulation-based estimates of the likelihood that a damaged building becomes unsafe under aftershocks for a range of possible safety thresholds, and (iii) explicitly incorporates multiple *EDP* types to represent the diverse ways structures develop and accumulate damage.

2.2. Overview of the proposed probabilistic framework

The probability that a damaged building is unsafe can be evaluated by calculating the likelihood that the collapse safety index κ does not exceed a predefined threshold $\kappa_{\min}$ for a given level of post-mainshock structural damage. This probability can be equivalently expressed as the likelihood that, for a given post-mainshock demand level represented by an *EDP*, that *EDP* exceeds the value corresponding to $\kappa_{\min}$, i.e.,

$$P_{\text{unsafe}} = P(\kappa \le \kappa_{\min} | EDP) = P\left(EDP \ge EDP_{\kappa_{\min}}\right) \tag{8}$$

where $EDP_{\kappa_{\min}}$ denotes the *EDP* corresponding to the residual collapse capacity threshold $\kappa_{\min}$. The complementary probability represents the likelihood that the mainshock-damaged building is safe for reoccupation. This probabilistic formulation implicitly incorporates record-to-record variability in both the collapse safety index κ and the *EDP* thresholds associated with each $\kappa_{\min}$.

2.2.1. Record-specific extraction of $\mathbf{EDP}_{\kappa_{\min}}$ for candidate $\boldsymbol{\kappa}_{\min}$ values

Seismic demands are notably affected by the polarity of aftershocks [6,20,36]. Accordingly, this study accounts for this effect in the evaluation of residual collapse capacity. For each ground-motion record i, κ_i is computed under positive and negative aftershock polarities (κ_{pp} and κ_{np}, respectively) and the conservative value $\kappa = \min(\kappa_{pp}, \kappa_{np})$ is retained. The polarity is considered positive when the aftershock acts in the same direction as the mainshock, and negative when it acts in the opposite direction. Furthermore, rather than adopting a single fixed value of $\kappa_{\min}$, as commonly done in previous studies, several candidate thresholds

Table 1
Limit states considered for *EDPs*.

Limit state	LS_1	LS_2	LS_3	LS_4	LS_5	LS_6	LS_7	LS_8
PIDR	0.002	0.007	0.015	0.025	0.0375	0.04	0.045	0.05
RIDR	0.001	0.002	0.005	0.01	0.015	0.02	0.03	0.04
DI	0.01	0.1	0.2	0.5	0.65	0.8	0.9	1.0

($\kappa_{\min}$ = 0.80, 0.85, 0.90, 0.95, and 0.98) are examined. For each candidate threshold $\kappa_{\min}$, the corresponding record-specific engineering demand parameter $EDP_{\kappa_{\min}}$, is obtained directly from the associated κ_i-EDP relationships. Specifically, $EDP_{\kappa_{\min}}$ is identified at the point where the record-specific κ_i-EDP curve reaches $\kappa_i = \kappa_{\min}$. Repeating this procedure for all records produces a set of $EDP_{\kappa_{\min},i}$ values for each candidate threshold and EDP type. This set preserves record-to-record variability in the demand associated with the specified residual collapse-capacity level and forms the basis for the subsequent probabilistic modeling.

2.2.2. Statistical modeling of $\boldsymbol{EDP_{\kappa_{\min}}}$

To estimate P_{unsafe} shown in Eq. (8), various statistical distributions, including Weibull, Normal, Lognormal, Beta, and Gamma, are fitted to a set of $EDP_{\kappa_{\min}}$ values based on each candidate threshold $\kappa_{\min}$. For each EDP type and candidate $\kappa_{\min}$, the parameters of all candidate distributions are estimated by maximum likelihood directly from the corresponding record-specific $EDP_{\kappa_{\min}}$ observations. Thus, the distributions are fitted to the observed EDP data rather than to the empirical cumulative or exceedance probabilities. The empirical CDF is represented as a right-continuous step function, whereas the fitted parametric CDFs are represented by continuous curves. The best-fitting distribution is then identified using goodness-of-fit (GOF) tests, including the Kolmogorov–Smirnov (K–S) test [37–40]. The K–S test compares the empirical cumulative distribution function (CDF) of the observed data with the theoretical CDF of a candidate distribution. In this study, the K–S statistic is used as a relative goodness-of-fit measure to compare the candidate distributions, rather than as a formal hypothesis test based on a selected significance level. The statistic D_n represents the maximum absolute difference between the theoretical cumulative distribution function, $F_X(x)$, and the empirical cumulative distribution function, $S_n(x)$, as defined in Eq. (9). The distribution yielding the smallest D_n is selected as the best-fitting distribution among the considered candidates.

$$D_n = \max_x |F_X(x) - S_n(x)| \tag{9}$$

After selecting the most suitable distribution for each EDP based on the K–S test, supplementary analyses are conducted to further assess model adequacy and parameter stability. The Anderson–Darling (AD) test [41] is applied as a tail-sensitive goodness-of-fit diagnostic, while nonparametric bootstrap resampling with 1000 resamples is used to quantify the sampling uncertainty and stability of the estimated distribution parameters. The point estimates obtained from the complete dataset are used in the subsequent probabilistic analyses, while the bootstrap-based 95% confidence intervals and coefficients of variation are used to evaluate the robustness of these estimates.

2.2.3. Computation of conditional probabilities

The probability that a damaged building becomes unsafe for a given threshold $\kappa_{\min}$ is obtained directly from the fitted cumulative distribution function (CDF) of the corresponding EDP values:

$$p_{i,\kappa_{min}} = P\left(EDP \geq EDP_{\kappa_{\min}}\right) = F_{EDP_{\kappa_{min}}}(EDP_i) \tag{10}$$

where $EDP_{\kappa_{\min}}$ is the EDP value associated with the residual collapse-capacity ratio κ equal to predefined threshold $\kappa_{\min}$, $F_{EDP_{\kappa_{\min}}}(\cdot)$ denotes the CDF fitted to the ensemble of EDP values corresponding to $\kappa_{\min}$, while EDP_i refers to the post-mainshock engineering demand parameter measured (or estimated) for a given building. This formulation allows the likelihood of unsafety to be evaluated for any observed damage state using the fitted distribution associated with the chosen threshold $\kappa_{\min}$.

2.2.4. Safety evaluation across a spectrum of $\boldsymbol{\kappa_{\min}}$ thresholds

Instead of prescribing a single $\kappa_{\min}$, the framework evaluates a range of plausible thresholds and quantifies how each choice affects the probability of aftershock-induced unsafety.

For every candidate $\kappa_{\min}$ within the considered range, the methodology yields a corresponding $EDP_{\kappa_{\min}}$ and its fitted distribution, from which the conditional unsafety probability $p_{(i,\kappa_{\min})}$ is computed using Eq. (10). By assembling these probabilities over all $\kappa_{\min}$ values, the framework produces a probabilistic safety profile, illustrating how conservative or permissive each threshold would be in practice.

Visualizing the variation of $p_{i,\kappa_{min}}$ across the $\kappa_{\min}$ spectrum provides a transparent and statistically consistent basis for understanding the implications of different safety thresholds. The bootstrap analysis is used separately to assess the sampling uncertainty and stability of the fitted distribution parameters, as reported through their 95% confidence intervals and coefficients of variation. Rather than prescribing a single $\kappa_{\min}$, the method equips engineers and policymakers with the information needed to select a threshold aligned with their risk tolerance, operational constraints, and desired level of conservatism in post-mainshock reoccupation decisions.

2.2.5. Safety decision for post-mainshock reoccupation

The final step of the framework involves evaluating the safety of a mainshock-damaged building for reoccupation. For each EDP type, the probability of safety corresponding to a given measured or estimated post-mainshock demand is computed as:

$$P_{\text{safe}} = 1 - P\left(EDP \geq EDP_{\kappa_{\min}}\right) \tag{11}$$

The $\kappa_{\min}$ used to define $EDP_{\kappa_{\min}}$ is selected from the candidate thresholds considered in this study (0.80, 0.85, 0.90, 0.95, and 0.98), according to the desired level of safety conservatism and stakeholder risk tolerance. This probability represents the likelihood that the mainshock-damaged building retains sufficient residual capacity to withstand potential aftershocks without collapse. A decision threshold p_{th} is introduced to formalize safety classification. The value of p_{th} can be defined by decision-makers or stakeholders to reflect risk tolerance, occupancy importance, or regional safety policies. The reoccupation decision rule is expressed as:

$$\begin{cases} P_{\text{safe}} \geq p_{th}, \text{Safe} \\ P_{\text{safe}} < p_{th}, \text{Unsafe} \end{cases} \tag{12}$$

To ensure a conservative and performance-consistent reoccupation decision, the safety evaluation must be satisfied across all demand measures. Since $PIDR$, $RIDR$, and DI capture different aspects of structural response (peak deformation, residual deformation, and cumulative damage), a building can be considered safe only when the safety probability implied by each EDP exceeds the target threshold. This requirement resolves conflicting outcomes among the demand measures through a conservative decision rule, thereby reducing the likelihood of a false-safe classification when any individual EDP indicates an unsafe condition. Thus, the reoccupation decision is governed by a logical AND condition applied simultaneously to the three safety probabilities, as expressed in Eq. (13).

$$P_{\text{safe},j} \geq p_{th,} \ \forall j \in \{PIDR, RIDR, DI\}\text{f} \tag{13}$$

If any of the three $EDPs$ yields a safety probability below p_{th}, the building is classified as unsafe, regardless of the values obtained from the remaining indicators. This joint decision rule provides a practical and conservative framework that reduces the likelihood of falsely declaring the structure safe based on a single performance metric.

2.2.6. Information required for building-specific implementation

Application of the proposed framework to a specific building requires both pre-earthquake analytical preparation and post-earthquake response information. During the pre-earthquake stage, an as-built nonlinear structural model must be developed using the building geometry, member and material properties, mass distribution, damping, nonlinear deterioration characteristics, and relevant second-order effects. Fig. 1 summarizes the overall computational framework and

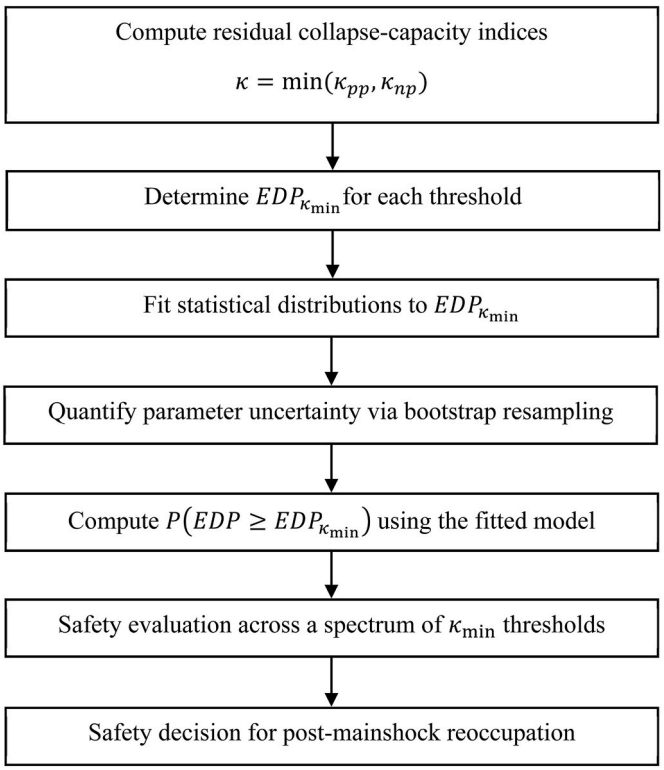

Fig. 1. Flowchart illustrating the probabilistic assessment framework based on $EDP_{\kappa_{\min}}$

provides context for the building-specific implementation requirements discussed in this section.

Site-specific seismic-hazard information and a representative suite of mainshock–aftershock records are then required to perform sequential analyses of the intact and damaged structure. These analyses generate the record-specific κ–EDP relationships, the statistical distributions of $EDP_{\kappa_{\min}}$, and the corresponding safety-probability relationships for the considered $\kappa_{\min}$ values. For a selected probability threshold p_{th}, these models are further used to derive the building-specific critical-demand relationships $EDP_{\text{crit}}(\kappa_{\min})$, which define the maximum admissible *PIDR*, *RIDR*, and *DI* values satisfying the prescribed safety requirement. These precomputed relationships can be stored as probability curves or lookup tables for rapid post-event use.

Following an earthquake, the required event-specific inputs are the measured or estimated *PIDR*, *RIDR*, and *DI* of the damaged building. *PIDR* may be obtained from recorded structural-response histories or reconstructed using a calibrated analytical model, whereas *RIDR* may be obtained from recorded or surveyed permanent floor displacements. *DI* requires reconstruction of the deformation and hysteretic-energy response using instrumentation or a calibrated analytical model. The measured EDPs are compared with the corresponding precomputed $EDP_{\text{crit}}(\kappa_{\min})$ values for the authority-selected $\kappa_{\min}$ and p_{th}. The building is considered eligible for reoccupation only when the measured values remain below the corresponding critical values for all considered EDPs. The resulting classification is intended to support, rather than replace, post-earthquake field inspection.

3. Case study

3.1. Structural modeling

To demonstrate the application of the proposed framework, a four-story, three-bay steel special moment frame (SMF) from an archetype office building developed by Elkady and Lignos [42] is analyzed. Plan and elevation views of the original building are shown in Fig. 2(a) and (b), respectively. The total building height is 16.6 m, with a first-story height of 4.6 m and typical upper-story heights of 4.0 m. Although the structure was originally designed according to U.S. seismic provisions, it is used here to evaluate the framework under the seismic hazard conditions relevant to Vancouver. This approach leverages a well-documented structural configuration while allowing for exploration of regional hazard-specific performance. The first-mode period, obtained through eigenvalue analysis, is 1.55 s. Further design details are provided in Refs. [43,44].

The nonlinear behavior of beams and columns is modeled using rotational springs based on the modified Ibarra-Medina-Krawinkler (IMK) deterioration model [45]. A leaning column is added to simulate P-Delta effects. Panel zones at the beam-column joints are represented by four rigid elastic beam-column elements, each incorporating a rotational spring at one corner to capture shear distortion under lateral loading.

A two-dimensional structural model is developed in OpenSees [46] based on findings showing good agreement between nonlinear dynamic analyses and shake table tests [47]. The parameters of the modified IMK model, such as the cyclic deterioration rate Λ, pre-capping rotation capacity θ_p, and post-capping plastic rotation capacity θ_{pc}, are determined using the empirical equations developed by Lignos and Krawinkler [48, 49], and adopted in PEER/ATC 72-1 [50]. The flexibility of beam-to-column joint panel zones is modeled following the recommendations of Gupta [51]. Equivalent damping is represented as a linear combination of stiffness-proportional and mass-proportional components (Rayleigh damping). A critical damping ratio (ξ) of 2% is applied to the first and third vibration modes, as recommended in PEER/ATC 72-1. The member sizes for the frame are defined in Table 2.

3.2. Seismicity of the site location

Southwestern Canada and the Northwestern United States are seismically active regions shaped by complex tectonic conditions. The seismic hazard in Vancouver originates from three primary sources: shallow crustal earthquakes, deep inslab events, and megathrust interface earthquakes from the Cascadia subduction zone. Crustal earthquakes occur at shallow depths (5–20 km) within the continental plate and can cause significant damage due to their proximity to urban areas. Their moment magnitudes are typically moderate to large (M_w 5.5 to 7.5). In contrast, inslab earthquakes occur within the subducting Juan de Fuca Plate, whereas interface earthquakes occur along the boundary between the Juan de Fuca and North American plates.

Interface events, resulting from a sudden release of accumulated strain, can exceed M_w 8. These three earthquake types exhibit distinct ground motion characteristics. Interface earthquakes generally produce longer-duration shaking and exhibit distinct spectral content due to differences in magnitude and source distance. Given the diversity of seismic sources affecting Vancouver, selecting appropriate ground motions is critical for a realistic assessment of building performance.

3.3. Ground motion selection

Accurate seismic assessment depends heavily on selecting ground motions that realistically represent the site-specific seismic hazard [52]. Various ground motion selection methods have been proposed in the literature (e.g., Refs. [53–56]). In this study, earthquake records are selected using a multiple conditional mean spectrum (CMS) approach [54], incorporating site-specific seismic hazard characteristics and the contributions of different earthquake sources, following the methodologies presented in Refs. [57–59].

The CMS-based method is particularly effective for capturing the seismic characteristics of multiple earthquake sources at a given site [60]. Key inputs for constructing the CMS and selecting ground motion records include the uniform hazard spectrum (UHS) corresponding to a

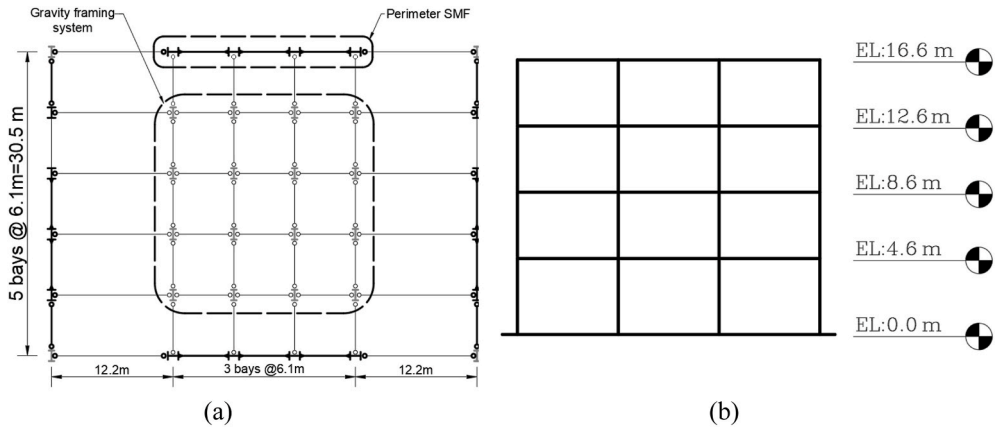

Fig. 2. Case-study steel office building: (a) plan view; and (b) elevation view.

Table 2
Selected frame member sections.

Story	Beam size	Column size		Doubler plate thickness [mm]	
		Exterior	Interior	Exterior	Interior
4	W21x57	W24x62	W24x62	0.0	7.9
3	W21x57	W24x103	W24x103	0.0	7.9
2	W21x57	W24x103	W24x103	0.0	7.9
1	W21x57	W24x103	W24x103	0.0	7.9

specific return period (2475 years in this study), as well as the results of seismic disaggregation. Disaggregation identifies earthquake scenarios, defined by mean magnitude and distance, that contribute the most significantly to seismic hazard, and quantifies the relative contributions of different seismic sources (crustal, interface, and inslab).

To characterize the seismic hazard from contributing sources, a probabilistic seismic hazard analysis (PSHA) is performed using a synthetic earthquake catalog. The fundamental period of the structure ($T_1 = 1.55$ s) is selected as the conditioning (anchor) period for the CMS. To identify records compatible with the target CMS, a comprehensive dataset of 731 mainshock-aftershock (MS-AS) sequences was assembled from multiple sources. This includes 172 sequences from the PEER-NGA database [61], 531 sequences from the Japanese K-NET, KiK-net, and SK-net databases [62,63], and 28 sequences from the 2016 Kumamoto earthquakes, also obtained from the Japanese K-NET and KiK-net databases. The dataset comprises 275 crustal, 340 interface, and 116 inslab events, ensuring adequate coverage for selecting appropriate records based on event type, magnitude, and distance. It is worth noting that the Japanese database contains records from the 2011 Tohoku earthquake, which are considered suitable surrogates for Cascadia subduction events. Additional information on the selected records can be found in Refs. [60,64–66]. The CMS method is then applied to select a set of 33 MS-AS seismic record sequences, including 11 crustal, 11 interface, and 11 inslab events.

The record selection and subsequent analyses use unidirectional ground-motion components. While bidirectional seismic excitation may influence structural response, damage accumulation and collapse capacity, the proposed framework itself is formulated independently of the loading direction and relies on the probabilistic characterization of engineering demand parameters (EDPs) and residual collapse capacity. Consequently, the methodology can be extended to bidirectional analyses by employing appropriate bidirectional ground-motion records and corresponding EDP-collapse relationships.

For the present case study, the investigation is limited to the response of a regular planar steel special moment frame in a single direction; unidirectional excitation is thus considered reasonable for demonstrating the proposed methodology. The results presented herein should therefore be interpreted within the context of the unidirectional analyses performed for the considered structure.

Fig. 3(a)–(c) present the target CMS along with the CMS ± standard deviation (SD), where SD is the conditional standard deviation as defined by Jayaram et al. [67]. These figures also show the response spectra of the selected scaled records, including the median, 16th percentile, and 84th percentile. Only mainshocks are considered in the CMS-based selection process, with the anchor period set to 1.55 s. The corresponding aftershocks are then taken directly from the same recorded mainshock–aftershock pairs, consistent with established practice in MS-AS studies, thereby preserving the physical consistency of the sequence [57–59]. The response spectra of the selected records for crustal and interface events closely match the target CMS. For inslab records, the selected records exhibit a greater concentration of short-period spectral content compared with the target. The final dataset includes 33 mainshocks and 33 associated aftershocks. Because the CMS-based selection is conditioned on the fundamental period ($T_1 = 1.55$ s), the target spectrum and the median spectrum of the selected records match at this period.

The mainshocks produce damaging ground motions that initiate varying damage states, while aftershocks represent subsequent excitations that may lead to the collapse of both intact and damaged buildings. Fig. 3(d) illustrates the distribution of magnitude versus epicentral distance for all selected mainshocks and the corresponding aftershock records.

4. Application of the probabilistic framework to the case study

4.1. Collapse safety index and extraction of $EDP_{\kappa_{min}}$

The collapse safety index, κ, is computed using Eq. (1), where *IM* is the average spectral acceleration proposed by Eads et al. [31] and calculated according to Eq. (2). As previously noted, both positive and negative aftershock polarities (κ_{np} and κ_{pp}) are considered to compute κ for different post-mainshock damage states. These calculations are performed using three *EDPs*, including *PIDR*, *RIDR*, and *DI*, as summarized in Table 1. The final value of κ is defined as the minimum of κ_{pp} and κ_{np}.

As discussed previously, a minimum acceptable residual collapse capacity, $\kappa_{\min}$, is adopted as a safety threshold. When $\kappa \leq \kappa_{\min}$, the mainshock-damaged building is considered unsafe for reoccupation. Fig. 4 illustrates the variation of the collapse safety index κ with different types of post-mainshock engineering demand parameters (*EDPs*) for all records, assuming $\kappa_{\min} = 0.85$.

For each record, the collapse-level κ computed from Eq. (1) is linked to its corresponding post-mainshock *EDP* value, resulting in κ–EDP data pairs used for subsequent analysis. The horizontal dashed line denotes

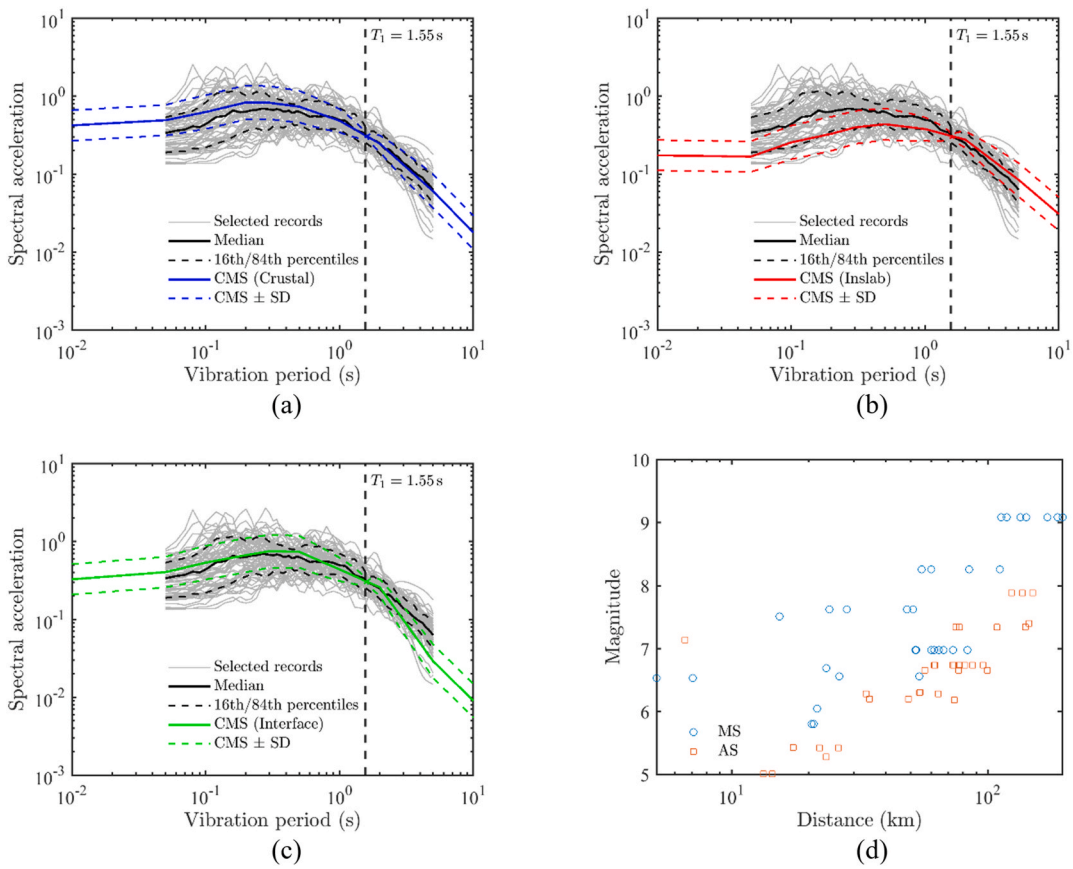

Fig. 3. Spectra of selected mainshock records with variability, median spectrum, target CMS, and CMS ± SD conditioned on the fundamental period of the 4-story SMF for: (a) crustal; (b) interface; (c) inslab earthquakes; and (d) magnitude–distance distribution of selected mainshocks and major aftershocks.
Note: MS = mainshocks; AS = aftershocks.

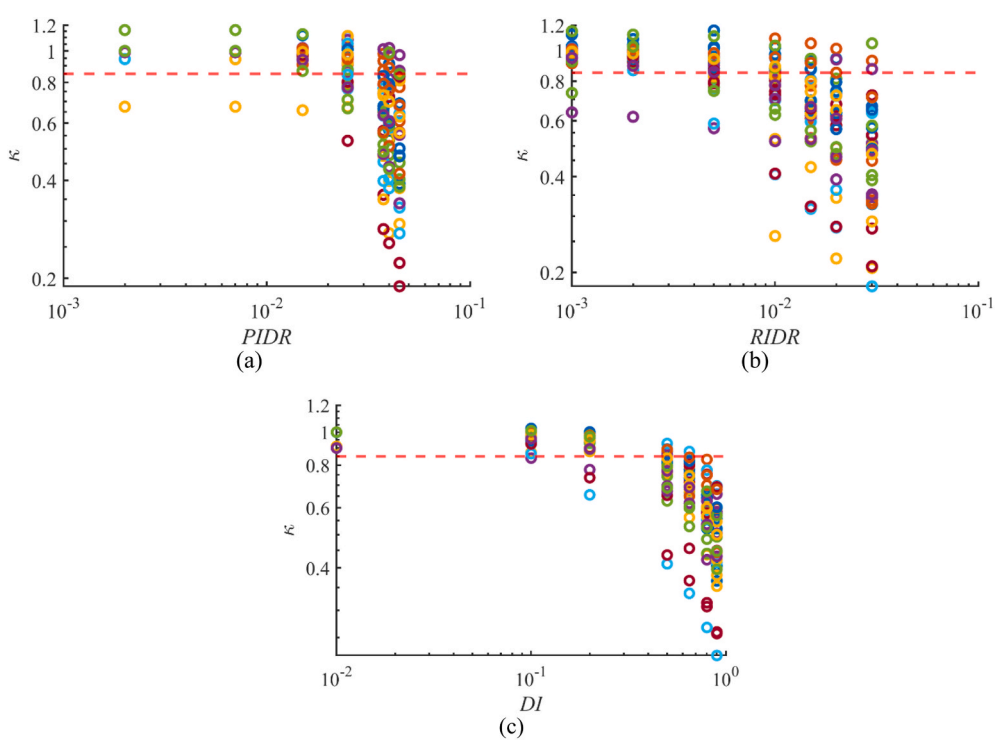

Fig. 4. Record-to-record variability of κ–EDP relationships for (a) PIDR, (b) RIDR, and (c) DI. The dashed red line indicates $\kappa_{\min} = 0.85$; hollow, color-coded markers represent individual records. (For interpretation of the references to color in this figure legend, the reader is referred to the Web version of this article.)

the selected safety threshold, and its intersections with the κ–*EDP* data identify the corresponding set of $EDP_{\kappa_{\min}}$ values. The results show that the choice of *EDP* strongly influences whether a damaged building satisfies the safety criterion and reveal significant record-to-record variability, underscoring the need for a probabilistic treatment of this uncertainty in the subsequent analysis.

Although values of $\kappa > 1$ may appear counterintuitive, this behavior has been widely reported (e.g., Refs. [24,27,68]). Such cases occur when the mainshock alters the structural deformation path so that the aftershock triggers a different, less critical collapse mechanism, sometimes corresponding to a "resurrection" branch of the IDA curve with higher effective capacity. In some instances, the aftershock may load the structure in the opposite direction of the mainshock or excite different vibration modes due to changes in frequency content, partially relieving residual deformations. These mechanisms can result in an apparent increase in collapse capacity after damage, rather than consistent degradation.

4.2. Probabilistic modeling and uncertainty quantification

A probabilistic framework is employed to evaluate the safety of mainshock-damaged buildings based on the engineering demand parameters (EDPs) associated with a minimum acceptable collapse safety index, denoted $EDP_{\kappa_{\min}}$. The probability of exceeding this limit state, $P(EDP \geq EDP_{\kappa_{\min}})$, is estimated by fitting candidate statistical distributions to the $EDP_{\kappa_{\min}}$ values. To reflect different levels of acceptable residual collapse capacity, five safety thresholds are considered: $\kappa_{\min} = 0.80$, 0.85, 0.90, 0.95, and 0.98. Decision makers may select the appropriate threshold according to the desired conservatism.

To identify the best-fitting distributions for the EDPs, Figs. 5–9 first visually compare the empirical and fitted CDFs for PIDR, RIDR, and DI at each level. To quantitatively assess these fits, several candidate cumulative distribution functions (CDFs) are then evaluated using the Kolmogorov–Smirnov (K–S) goodness-of-fit test. The distributions considered are Normal, Lognormal, Beta, Gamma, and Weibull. The corresponding reductions in residual collapse capacity, relative to the undamaged case, are 20%, 15%, 10%, 5%, and 2% for $\kappa_{\min} = 0.80$, 0.85, 0.90, 0.95, and 0.98, respectively. Among these, $\kappa_{\min} = 0.98$ represents the most conservative threshold. As observed in Figs. 5–9, the Weibull distribution closely matches the empirical CDFs for the three EDPs and the investigated $\kappa_{\min}$ levels. This is particularly evident in the central portion of the distributions, while slight deviations may occur in the tail regions for some cases. In contrast, the Normal, Lognormal, Beta, and Gamma distributions exhibit larger discrepancies from the empirical CDFs for several EDP–$\kappa_{\min}$ combinations.

Tables 3–7 present K–S test statistics for each candidate distribution and $\kappa_{\min}$ value, where lower values indicate better fit with empirical data. The visual observations from Figs. 5–9 are further confirmed by the K–S test results. Overall, the Weibull distribution yields the lowest or among the lowest K–S statistics for the majority of the examined cases and consistently provides a reliable representation of the $EDP_{\kappa_{\min}}$ data across the three EDP types and the investigated $\kappa_{\min}$ levels. Therefore, the Weibull distribution is adopted in the subsequent probabilistic analyses.

The probability density function (PDF) and cumulative distribution function (CDF) of the two-parameter Weibull distribution used in this study are given in Eqs. (14) and (15) [69,70].

$$f(\upsilon) = \frac{\beta}{\eta}\left(\frac{\upsilon}{\eta}\right)^{\beta-1} e^{-(\upsilon/\eta)^{\beta}} \tag{14}$$

$$F(\upsilon) = 1 - e^{-(\upsilon/\eta)^{\beta}} \tag{15}$$

where υ is the engineering demand parameter corresponding to $EDP_{\kappa_{\min}}$, β is the shape parameter ($\beta > 0$), and η is the scale parameter ($\eta > 0$). The parameters β and η are estimated using the maximum likelihood estimation (MLE) method.

To further evaluate the robustness and stability of the Weibull fit, a bootstrap resampling analysis is conducted using 1000 replicates for

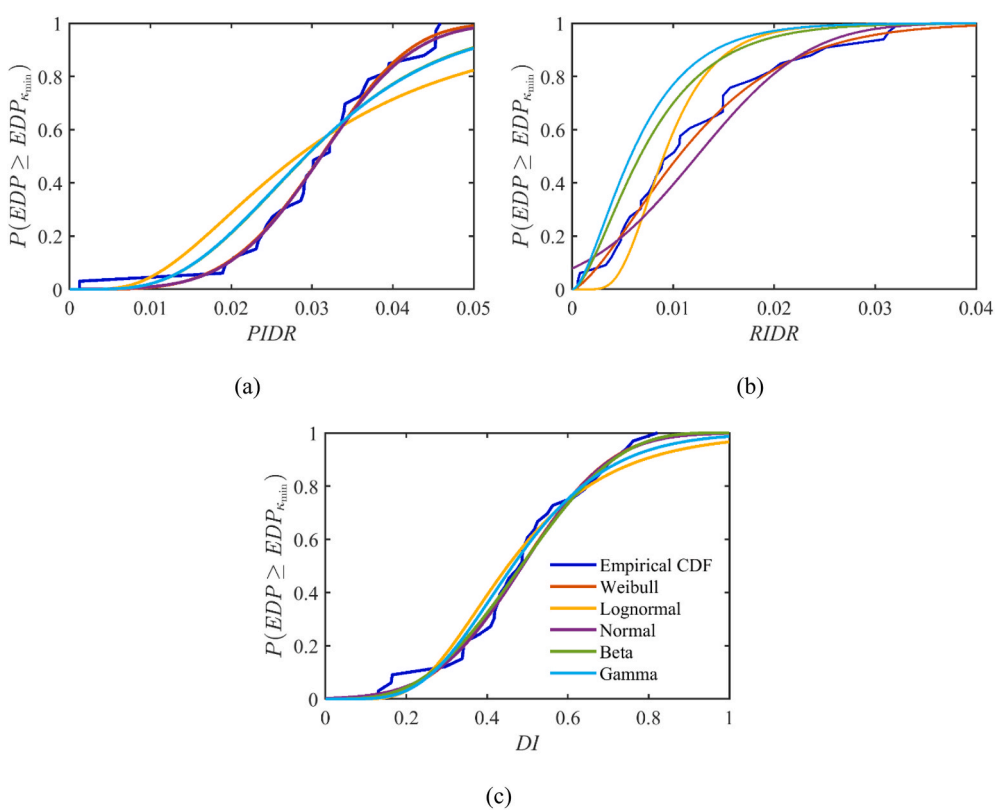

Fig. 5. Stepwise empirical CDF and fitted parametric CDFs, when $\kappa_{\min} = 0.80$, considering different distributions for: (a) *PIDR*, (b) *RIDR*, and (c) *DI*.

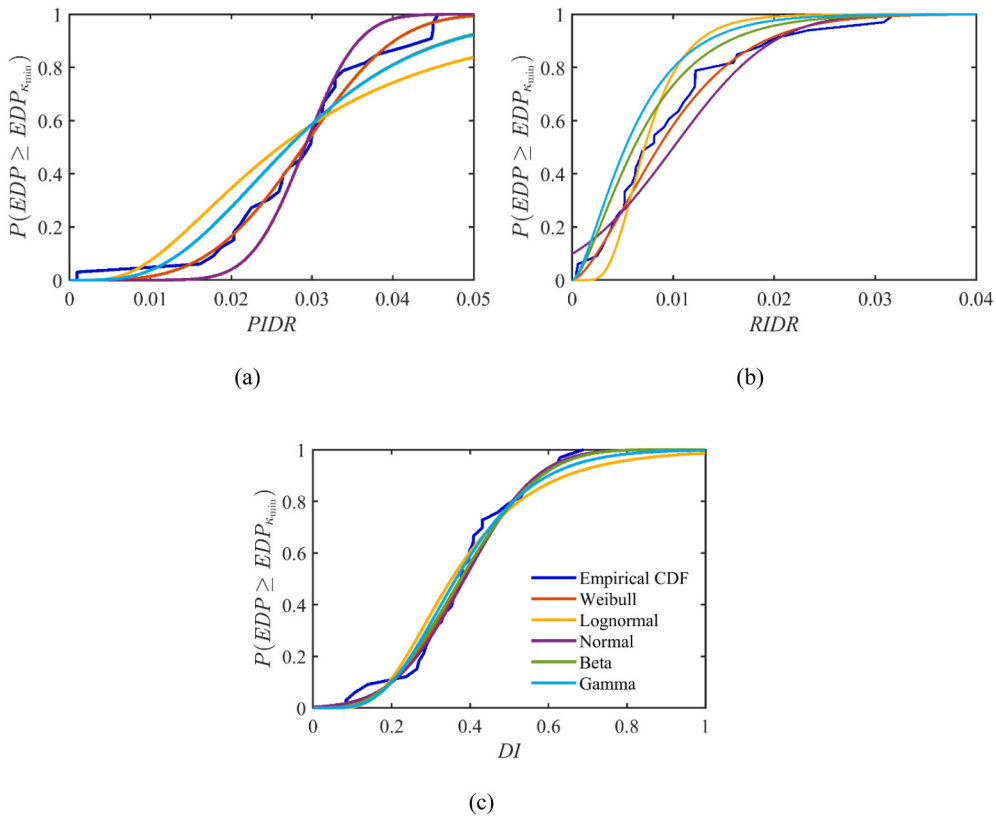

Fig. 6. Stepwise empirical CDF and fitted parametric CDFs, when $\kappa_{\min} = 0.85$, considering different distributions for: (a) *PIDR*, (b) *RIDR*, and (c) *DI*.

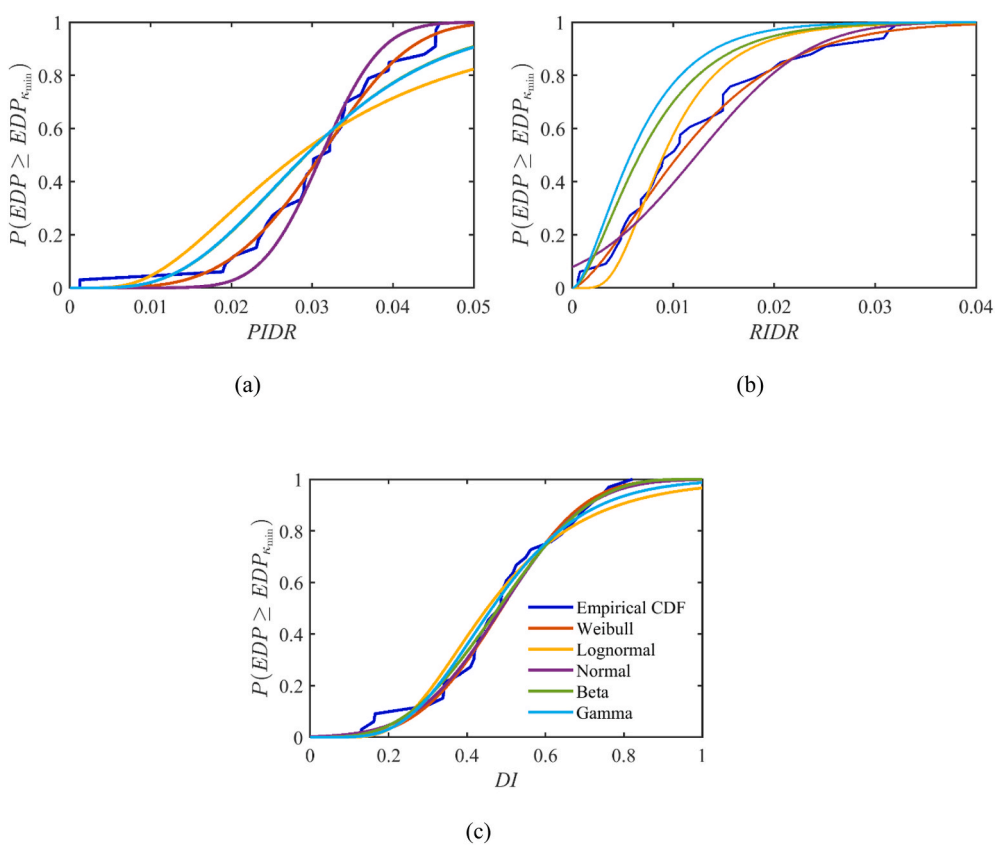

Fig. 7. Stepwise empirical CDF and fitted parametric CDFs, when $\kappa_{\min} = 0.90$, considering different distributions for: (a) *PIDR*, (b) *RIDR*, and (c) *DI*.

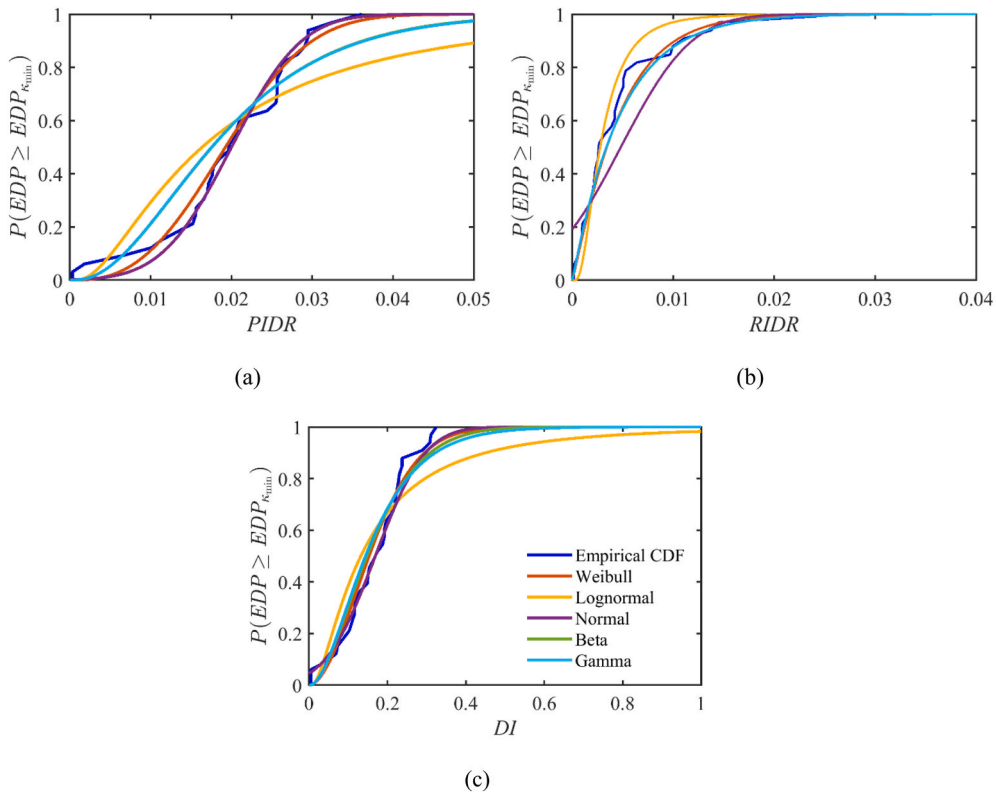

Fig. 8. Stepwise empirical CDF and fitted parametric CDFs, when $\kappa_{\min} = 0.95$, considering different distributions for: (a) *PIDR*, (b) *RIDR*, and (c) *DI*.

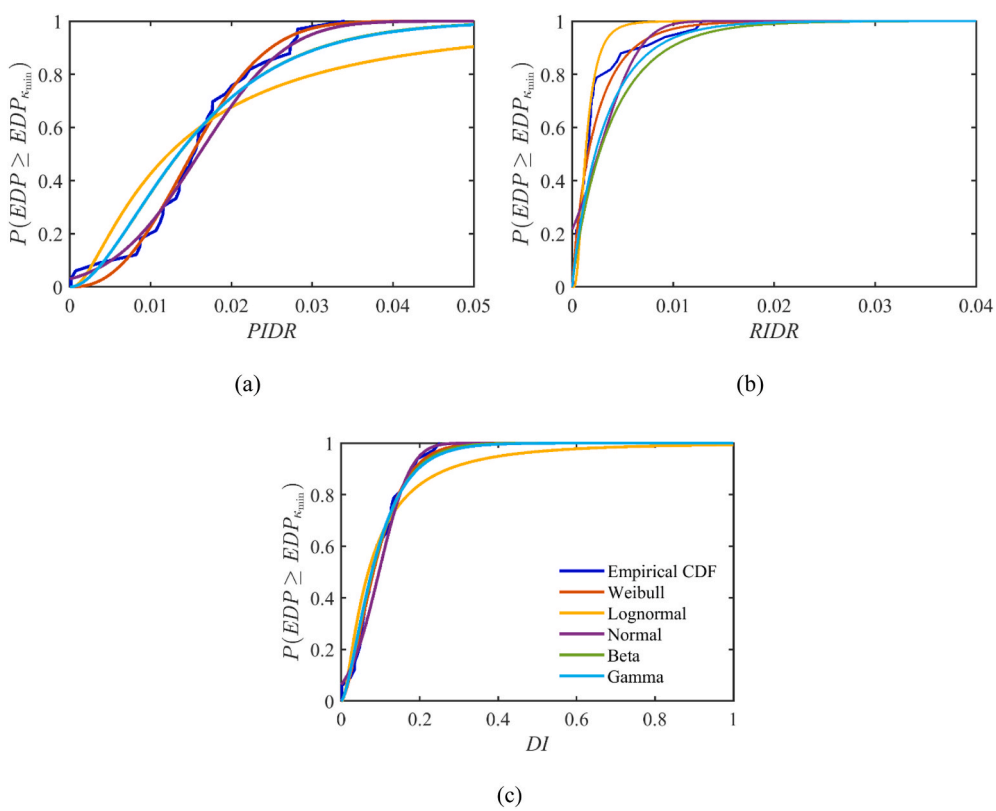

Fig. 9. Stepwise empirical CDF and fitted parametric CDFs, when $\kappa_{\min} = 0.98$, considering different distributions for: (a) *PIDR*, (b) *RIDR*, and (c) *DI*.

each EDP–$\kappa_{\min}$ combination. For each resample, the Weibull shape (β) and scale (η) parameters are re-estimated, allowing for the derivation of 95% confidence intervals (*CIs*) and coefficients of variation (*COVs*) to quantify parameter uncertainty.

Table 3
K–S statistics for different distributions and *EDPs*, when $\kappa_{\min} = 0.80$

K–S statistics	Weibull	Lognormal	Normal	Beta	Gamma
PIDR	0.0881	0.2503	0.0885	0.1835	0.1856
RIDR	0.0670	0.2378	0.1512	0.2344	0.3081
DI	0.0804	0.1678	0.0815	0.0989	0.1365

Table 4
K–S statistics for different distributions and *EDPs*, when $\kappa_{\min} = 0.85$

K–S statistics	Weibull	Lognormal	Normal	Beta	Gamma
PIDR	0.0890	0.2336	0.1699	0.1626	0.1645
RIDR	0.0957	0.1062	0.1781	0.18019	0.24781
DI	0.0965	0.1496	0.1041	0.1039	0.1178

Table 5
K–S statistics for different distributions and *EDPs*, when $\kappa_{\min} = 0.90$

K–S statistics	Weibull	Lognormal	Normal	Beta	Gamma
PIDR	0.0887	0.2503	0.1372	0.1836	0.1856
RIDR	0.0703	0.1958	0.1512	0.2344	0.3088
DI	0.0795	0.1678	0.0811	0.1074	0.1365

Table 6
K–S statistics for different distributions and *EDPs*, when $\kappa_{\min} = 0.95$

K–S statistics	Weibull	Lognormal	Normal	Beta	Gamma
PIDR	0.1366	0.2859	0.1547	0.2316	0.2329
RIDR	0.1128	0.1556	0.2521	0.1204	0.1228
DI	0.1203	0.2154	0.1259	0.1425	0.1550

Table 7
K–S statistics for different distributions and *EDPs*, when $\kappa_{\min} = 0.98$

K–S statistics	Weibull	Lognormal	Normal	Beta	Gamma
PIDR	0.0940	0.2673	0.1125	0.2005	0.2017
RIDR	0.1644	0.1776	0.3119	0.3257	0.2777
DI	0.0853	0.1841	0.1404	0.1099	0.1154

The results summarized in Tables 8–12 for $\kappa_{\min}$ ranging from 0.80 to 0.98 show that both Weibull parameters exhibit reasonably narrow 95% confidence intervals and relatively low coefficients of variation (COV < 0.3), indicating stable parameter estimates under resampling. The K–S and AD p-values reported in Tables 8–12 are calculated using the Weibull distribution parameterized by the bootstrap mean estimates. Because the distribution parameters are estimated from the same dataset, these values are interpreted as supplementary goodness-of-fit diagnostics rather than as formally calibrated hypothesis tests. All reported values exceed 0.05 and therefore provide no indication of a pronounced overall or tail-related lack of fit.

Overall, these results support the adequacy and robustness of the Weibull distribution for modeling the probabilistic variability of $EDP_{\kappa_{\min}}$ across all EDP types. Similar bootstrap-based parameter stability is observed across all investigated $\kappa_{\min}$ levels, further supporting the consistency of the Weibull model under different safety criteria. Tables 3–7 present K–S statistics used to compare the candidate distributions, whereas Tables 8–12 summarize bootstrap-based supplementary goodness-of-fit diagnostics and parameter uncertainty for the selected Weibull model at different levels of $\kappa_{\min}$.

The bootstrap results indicate that the estimated Weibull parameters remain reasonably stable under resampling, as reflected by their confidence intervals and coefficients of variation. Tables 8–12 summarize bootstrap-based parameter uncertainty and supplementary goodness-of-fit diagnostics. The complete-dataset Weibull parameter estimates are used to generate the subsequent probability and decision curves and are therefore not tabulated separately; the bootstrap-based confidence intervals are used only to assess parameter stability and are not propagated through these curves.

4.3. Probabilistic assessment of post-mainshock safety across $\kappa_{\min}$ thresholds

Fig. 10 compares the Weibull-derived exceedance-probability curves ($P(EDP \geq EDP_{\kappa_{\min}})$ for *PIDR*, *RIDR*, and *DI* across all considered $\kappa_{\min}$ levels. As $\kappa_{\min}$ increases, the probability of exceeding $EDP_{\kappa_{\min}}$ also increases, indicating that stricter safety thresholds correspond to a higher likelihood of a mainshock-damaged building being classified as unsafe under similar seismic demand. For example, when $PIDR = 0.02$, the exceedance probabilities are 0.0919, 0.1655, 0.2123, 0.5372, and 0.7444 for $\kappa_{\min} = 0.80$, 0.85, 0.90, 0.95, and 0.98, respectively, highlighting the influence of threshold selection and record-to-record variability. This trend implies that when residual collapse capacity reduction is used as a reoccupation criterion, even moderately damaged buildings may be deemed unsafe under more conservative thresholds.

Moreover, the derived unsafety probability, $P(EDP \geq EDP_{\kappa_{\min}})$, is sensitive to the choice of *EDP*. The probability approaches unity when $PIDR > 0.04$, $RIDR > 0.025$, and $DI > 0.7$, indicating near certainty of exceeding the safety threshold and, therefore, a very low likelihood of reoccupation eligibility. These results highlight the need for a multi-parameter decision framework, as discussed in the following section, to enhance the robustness and reliability of post-earthquake safety evaluations.

4.4. Decision-making for reoccupation

The safety probability P_{safe}, computed using Eq. (11), represents the likelihood that the mainshock-damaged building is safe. As shown in Fig. 11, this probability decreases with increasing structural damage. For instance, when $DI = 0.4$, P_{safe} drops from 0.6881 to 0.00082 as $\kappa_{\min}$ increases from 0.80 to 0.98. This strong sensitivity highlights that the safety assessment is not only damage-dependent but also heavily influenced by the selected collapse-safety threshold $\kappa_{\min}$, which must ultimately be defined by decision-makers or stakeholders based on the building's importance, occupancy type, and regional post-earthquake reoccupation policies. The safety probability also varies across different engineering demand parameters (*EDPs*). For $\kappa_{\min} = 0.95$, for instance, a 50% safety probability corresponds to significantly different demand levels, $PIDR = 0.0194$, $RIDR = 0.0034$, and $DI = 0.1552$, demonstrating that the interpretation of structural condition is inherently tied to the selected performance metric. This underlines the importance of using multiple *EDPs* to achieve a more reliable representation of structural safety.

Table 8
Bootstrap-based 95% confidence intervals and coefficients of variation for the Weibull parameters, together with goodness-of-fit results for the three EDPs at $\kappa_{\min} = 0.80$.

EDP	95% *CI* for scale parameter η	95% *CI* for shape parameter β	*K–S p*	*AD–p*	*COV* (η)	*COV* (β)	Interpretation
PIDR	[0.030343, 0.037229]	[2.1437, 5.4791]	0.7586	0.5794	0.0508	0.2332	Good fit
RIDR	[0.010316, 0.01705]	[1.1567, 1.8937]	0.9946	0.9760	0.1310	0.1255	Good fit
DI	[0.48227, 0.59922]	[2.5037, 4.3351]	0.9435	0.8894	0.0568	0.1428	Good fit

Table 9
Bootstrap-based 95% confidence intervals and coefficients of variation for the Weibull parameters, together with goodness-of-fit results for the three EDPs at $\kappa_{\min} = 0.85$

EDP	95% *CI* for scale parameter η	95% *CI* for shape parameter β	*K–S p*	*AD–p*	*COV* (η)	*COV* (β)	Interpretation
PIDR	[0.028162, 0.035388]	[1.9448, 4.7635]	0.8727	0.5435	0.0573	0.2206	Good fit
RIDR	[0.0081969, 0.013993]	[1.0927, 1.8161]	0.8485	0.9501	0.1407	0.1307	Good fit
DI	[0.3791, 0.48031]	[2.3171, 4.0343]	0.8897	0.8899	0.0614	0.1462	Good fit

Table 10
Bootstrap-based 95% confidence intervals and coefficients of variation for the Weibull parameters, together with goodness-of-fit results for the three EDPs at $\kappa_{\min} = 0.90$

EDP	95% *CI* for scale parameter η	95% *CI* for shape parameter β	*K–S p*	*AD–p*	*COV* (η)	*COV* (β)	Interpretation
PIDR	[0.024926, 0.032138]	[1.7964, 4.4015]	0.6234	0.5231	0.0626	0.2247	Good fit
RIDR	[0.0058258, 0.010569]	[1.0032, 1.7812]	0.6987	0.9241	0.1505	0.1477	Good fit
DI	[0.25986, 0.35367]	[1.527, 3.3816]	0.5790	0.5149	0.0799	0.2022	Good fit

Table 11
Bootstrap-based 95% confidence intervals and coefficients of variation for the Weibull parameters, together with goodness-of-fit results for the three EDPs at $\kappa_{\min} = 0.95$

EDP	95% *CI* for scale parameter η	95% *CI* for shape parameter β	*K–S p*	*AD–p*	*COV* (η)	*COV* (β)	Interpretation
PIDR	[0.0186, 0.0252]	[1.42, 3.98]	0.343	0.313	0.0748	0.2626	Good fit
RIDR	[0.00322, 0.00666]	[0.80, 1.40]	0.709	0.904	0.1885	0.1456	Good fit
DI	[0.153, 0.218]	[1.30, 3.05]	0.685	0.465	0.0881	0.2166	Good fit

Table 12
Bootstrap-based 95% confidence intervals and coefficients of variation for the Weibull parameters, together with goodness-of-fit results for the three EDPs at $\kappa_{\min} = 0.98$

EDP	95% *CI* for scale parameter η	95% *CI* for shape parameter β	*K–S p*	*AD–p*	*COV* (η)	*COV* (β)	Interpretation
PIDR	[0.014309, 0.02065]	[1.1578, 3.0868]	0.4939	0.3568	0.0944	0.2409	Good fit
RIDR	[0.0015403, 0.0034602]	[0.74456, 1.214]	0.3002	0.6165	0.2123	0.1330	Good fit
DI	[0.081623, 0.13138]	[1.0699, 2.0873]	0.9530	0.8541	0.1211	0.1664	Good fit

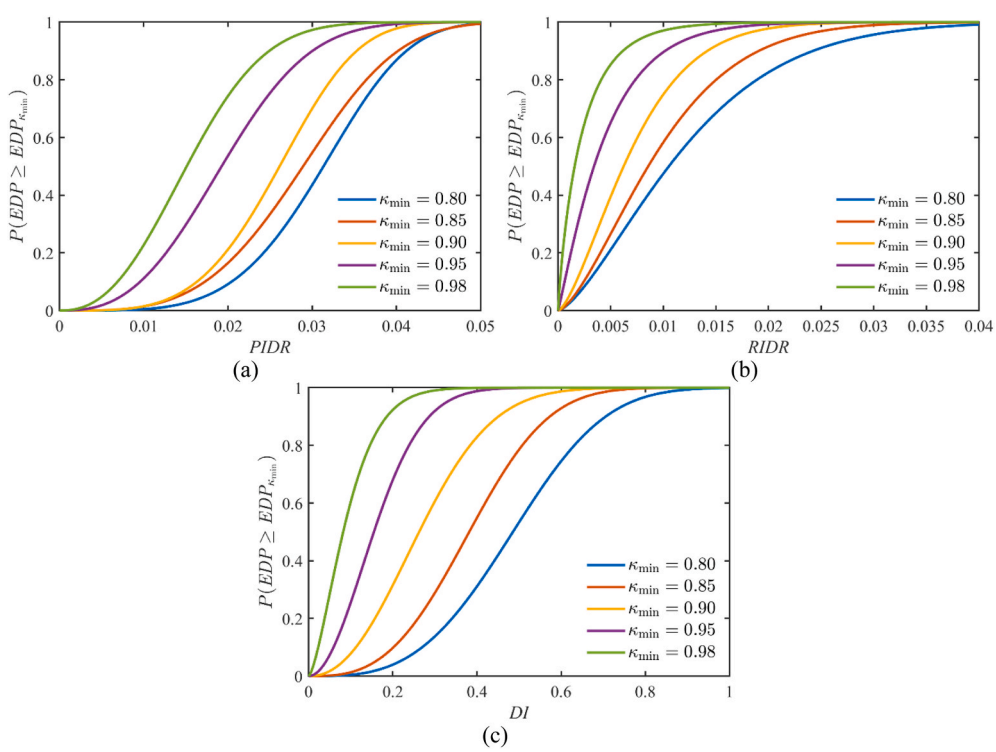

Fig. 10. Weibull-derived exceedance-probability curves for different $\kappa_{\min}$ levels: (a) *PIDR*, (b) *RIDR*, and (c) *DI*, considering all MS–AS events.

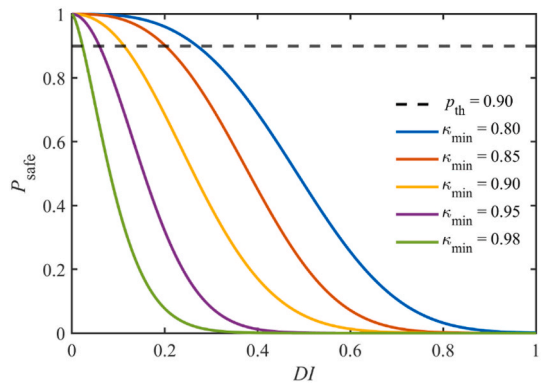

Fig. 11. Probability of safety, P_{safe}, as a function of the post-mainshock *DI* for various collapse-capacity thresholds.

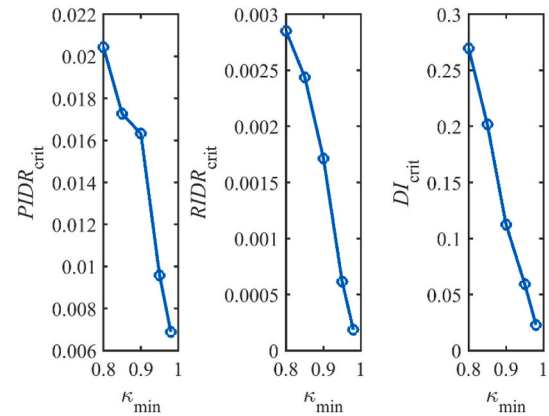

Fig. 12. Critical *EDP* levels, $EDP_{crit}(\kappa_{min})$, required to satisfy the safety condition $P_{safe} \geq 0.90$, shown for (a) *PIDR*, (b) *RIDR*, and (c) *DI*.

The reoccupation decision is formalized using Eqs. (12) and (13), where p_{th} is a safety probability threshold representing the minimum acceptable confidence level required for permitting re-entry. This threshold may be set by policymakers (e.g., $p_{th} = 0.90$ may represent a 90% safety-probability requirement) and reflects risk tolerance and societal expectations. In this study, $p_{th} = 0.90$ is adopted illustratively, corresponding to an allowable unsafety probability of 10%. This numerical correspondence is used only as an illustrative reference and should not be interpreted as a direct calibration or endorsement of the reoccupation threshold by FEMA P695 [71], which addresses mainshock collapse performance rather than post-earthquake reoccupation. The appropriate value of p_{th} should ultimately be established by the responsible authorities and stakeholders according to building importance, occupancy, acceptable risk, and regional post-earthquake policies.

Fig. 11 illustrates the probability that the mainshock-damaged structure is safe, P_{safe}, as a function of the observed damage index (DI) for multiple values of κ_{min}. Each curve corresponds to a different κ_{min} (0.80–0.98), showing how the safety probability decreases as damage accumulates and as stricter collapse-safety targets are imposed. For small *DI* values, all curves lie close to $P_{safe} \approx 1$, indicating that lightly damaged buildings are predicted to remain safe under further shaking. As *DI* increases, the curves progressively diverge; higher κ_{min} values (e.g., 0.95–0.98) drop much faster than the more permissive values (0.80–0.85). This demonstrates the strong sensitivity of safety decisions to the chosen collapse-capacity threshold.

The dashed horizontal line marks the safety-acceptance criterion $P_{safe} = p_{th} = 0.90$. The intersection of each curve with this line identifies the maximum *DI* for which the building is deemed safe under that specific κ_{min}. This graphical interpretation is directly useful for practice: an engineer measures or estimates the post-mainshock *DI* and obtains the corresponding P_{safe} from the curve associated with the selected κ_{min}, thereby providing rapid post-earthquake decision support.

For practical implementation, the computationally intensive building-specific nonlinear analyses and probabilistic calibration would be completed before an earthquake. These analyses would generate the safety-probability models and the $EDP_{crit}(\kappa_{min})$ relationships for *PIDR*, *RIDR*, and *DI* at the selected probability threshold p_{th}. Fig. 12 presents these precomputed critical-demand relationships for the case-study building at $p_{th} = 0.90$. Following an earthquake, the required event-specific inputs would be the measured or estimated post-mainshock *PIDR*, *RIDR*, and *DI*. These values would be compared with the corresponding precomputed critical values for the selected κ_{min} and p_{th}, providing the basis for the combined reoccupation assessment illustrated in Fig. 13.

These precomputed critical-demand relationships represent the maximum allowable *PIDR*, *RIDR*, and *DI* values for which the safety requirement $P_{safe} \geq p_{th} = 0.90$ is satisfied. Each subplot corresponds to one EDP type and shows how the reoccupation limit varies as the collapse-capacity threshold is tightened. A downward trend is observed as κ_{min} increases, indicating that the allowable deformation limits become more restrictive as higher residual collapse capacity is required. This figure provides stakeholders with a transparent and quantitative basis for selecting κ_{min}. For example, adopting a stringent $\kappa_{min} = 0.95$ tightens the reoccupation limits across all *EDPs*, whereas a more permissive $\kappa_{min} = 0.85$ allows substantially larger post-mainshock deformations before a structure is classified as unsafe. Thus, Fig. 12 quantifies the direct trade-off between targeted collapse safety and allowed post-mainshock deformation, which is central to policymaking for rapid reoccupation decisions. Since no single *EDP* fully characterizes post-mainshock performance, the safety evaluation is carried out for all three *EDPs* considered in this study (*PIDR*, *RIDR*, and *DI*). A building is deemed safe only when the safety requirement $P_{safe} \geq p_{th}$ is satisfied simultaneously for all three performance measures. This multi-parameter requirement reduces the likelihood of a false-safe classification that may occur when only one response metric is considered. By incorporating peak deformation, residual deformation, and cumulative damage simultaneously, the combined evaluation enhances the robustness of the assessment and provides a more reliable and transparent basis for post-earthquake reoccupation decisions.

Using the precomputed critical-demand relationships presented in Figs. 12 and 13 illustrates the final reoccupation decision framework by directly comparing illustrative measured or estimated post-mainshock EDPs, *PIDR**, *RIDR**, and *DI**, with their corresponding $EDP_{crit}(\kappa_{min})$ values. These critical values represent the maximum admissible demand that maintains a safety probability $P_{safe} \geq p_{th}$ for a given collapse-safety level κ_{min}. In the figure, the black markers identify the critical EDP values corresponding to the selected threshold $\kappa_{min} = 0.90$. The horizontal critical-demand thresholds passing through these markers define the acceptable and unsafe demand regions used in the illustrative reoccupation assessment. The blue curves in Fig. 13 show the precomputed $EDP_{crit}(\kappa_{min})$ relationships derived from the Weibull-based probabilistic models at the selected safety-probability threshold p_{th}. The red dashed lines indicate an illustrative example of measured or estimated post-mainshock EDPs, $PIDR^* = 0.015$, $RIDR^* = 0.002$, and $DI^* = 0.20$.

For the selected threshold $\kappa_{min} = 0.90$, the shaded region above each horizontal threshold line represents EDP values exceeding the corresponding critical demand $EDP_{crit}(0.90)$. These conditions correspond to $P_{safe} < p_{th}$, indicating that the damaged structure does not satisfy the required safety criterion and is therefore unsafe for reoccupation. A building is deemed safe only when all three measured or estimated EDPs fall below their respective critical-demand thresholds. This simultaneous requirement reflects the need for consistent safety across deformation-based, residual, and energy-based damage metrics.

As shown in Fig. 13(a), *PIDR** lies below the corresponding critical

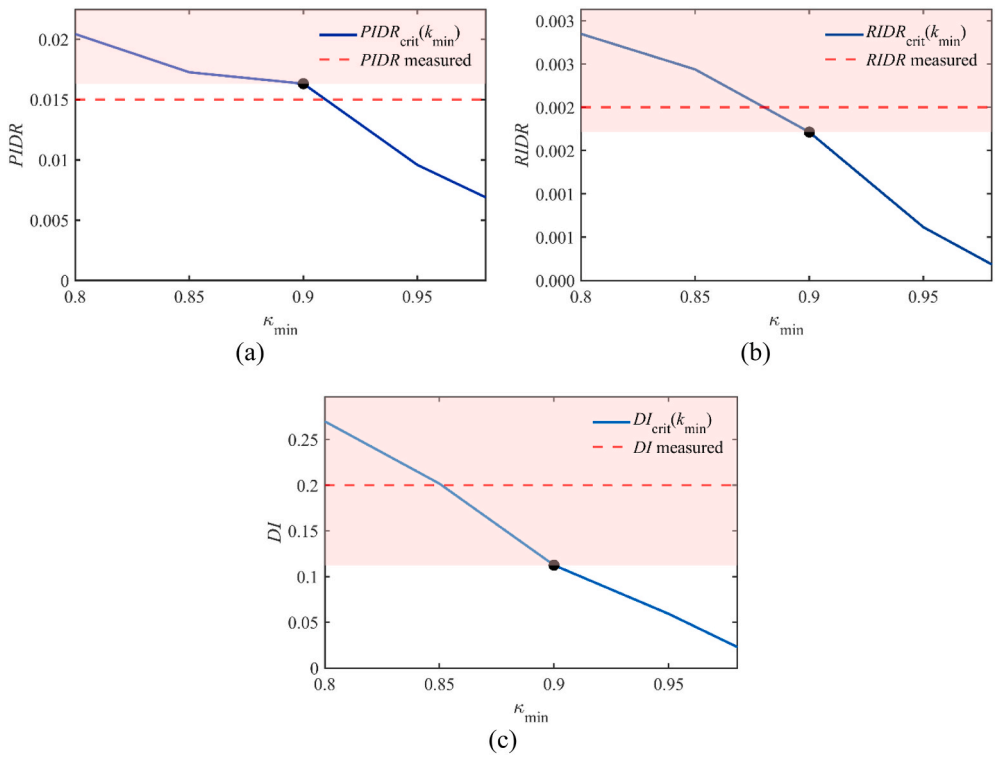

Fig. 13. Safety-based reoccupation thresholds for (a) peak drift (*PIDR*), (b) residual drift (*RIDR*), and (c) damage index (*DI*). The blue curves represent the precomputed critical-demand relationships, the black markers identify the critical values at the selected threshold $\boldsymbol{\kappa_{\min}} = 0.90$, and the red dashed lines indicate an example of measured or estimated post-mainshock EDPs. The shaded regions above the horizontal thresholds passing through the black markers represent unsafe demand levels for the selected $\boldsymbol{\kappa_{\min}} = \mathbf{0.90}$, for which $\boldsymbol{P_{\text{safe}}} < \boldsymbol{p_{\text{th}}}$. (For interpretation of the references to color in this figure legend, the reader is referred to the Web version of this article.)

threshold and remains outside the unsafe region. In contrast, $RIDR^*$ and DI^*, shown in Fig. 13(b) and (c), respectively, exceed their corresponding critical values and fall within the shaded unsafe regions. Therefore, despite acceptable transient drift, the structure does not satisfy the combined safety condition and is classified as unsafe for reoccupation at the selected $\kappa_{\min}$. Fig. 13 provides a practical and transparent decision tool: once the post-mainshock *PIDR*, *RIDR*, and *DI* have been measured or estimated, an engineer can compare them directly with the selected precomputed critical values and determine whether the building satisfies the required safety criterion.

The proposed probabilistic framework provides a structured basis for post-earthquake decision-making by quantifying the probability that the residual collapse capacity of a damaged building falls below an acceptable threshold. The proposed methodology differs from conventional post-earthquake assessment approaches, which commonly rely on a single engineering demand parameter and deterministic threshold checks, often based on median estimates of structural performance, and therefore do not explicitly account for uncertainty in the decision-making process. In contrast, the proposed methodology integrates multiple EDPs within a probabilistic assessment framework that explicitly represents record-to-record variability and provides a more comprehensive characterization of the structural condition. In the example shown in Fig. 13, consideration of *PIDR* alone would suggest acceptable performance, whereas the simultaneous consideration of *PIDR*, *RIDR*, and *DI* leads to an unsafe classification, highlighting the importance of incorporating multiple damage indicators in post-earthquake decision-making.

The framework incorporates regional seismic characteristics and ground motion variability, aligning with the principles of performance-based engineering. This approach can support the development of reoccupation guidelines and rapid safety screening tools following major seismic events. More broadly, the results underscore the need to integrate damage-dependent vulnerability metrics into seismic risk mitigation strategies and decision-support systems.

5. Summary and conclusions

This study presents a probabilistic framework for evaluating the safety of mainshock-damaged buildings subjected to subsequent aftershocks. To demonstrate the proposed methodology, incremental dynamic analyses were performed on a four-story steel special moment frame, considering both intact and mainshock-damaged configurations under a suite of aftershock ground motions. The framework incorporates three engineering demand parameters, peak inter-story drift ratio (*PIDR*), residual inter-story drift ratio (*RIDR*), and the Park–Ang damage index (*DI*), to capture different dimensions of structural response and damage.

Central to the framework is the collapse safety index, κ, which represents the ratio of the aftershock collapse capacity of the damaged structure to that of its intact state. A minimum acceptable limit, $\kappa_{\min}$, was defined to distinguish safe from unsafe post-mainshock conditions, with the exceedance of the corresponding EDP threshold, $EDP_{\kappa_{\min}}$, forming the basis of probabilistic safety assessment. Record-to-record variability in aftershock performance was explicitly incorporated through the probabilistic characterization of collapse capacity and *EDP* exceedance.

The results of this study lead to several key findings.

- The probability that a building is unsafe for reoccupation increases rapidly with more conservative $\kappa_{\min}$ values. This demonstrates how the selected safety thresholds, if set too high, may increase evacuation and downtime, even for buildings with only moderate damage. This finding is directly relevant for post-earthquake recovery

policies, where balancing safety, resilience, and continuity of service is critical.

- The choice of EDP plays a central role in safety evaluation because *PIDR*, *RIDR*, and *DI* capture different aspects of structural response. In the illustrative reoccupation assessment, consideration of *PIDR* alone indicates acceptable performance, whereas *RIDR* and *DI* lead to an unsafe classification. This suggests that relying solely on peak drift may overestimate post-mainshock safety by failing to capture residual deformation and cumulative damage. Accordingly, integrating deformation-, residual-, and cumulative-damage indicators provides a more comprehensive assessment of structural safety.
- The two-parameter Weibull distribution consistently provides a good statistical fit for modeling the exceedance probability of $EDP_{\kappa_{\min}}$, across all EDP types and $\kappa_{\min}$ levels, offering a coherent basis for quantifying uncertainty in collapse capacity.
- Exploration of different $\kappa_{\min}$ values shows that the allowable EDP limits depend strongly on the selected $\kappa_{\min}$. Because $\kappa_{\min}$ represents the minimum acceptable residual collapse capacity, its selection is inherently decision-dependent and should be established by relevant stakeholders based on risk tolerance, building importance, occupancy, and the desired level of safety conservatism.
- Safety evaluation across a wide spectrum of $\kappa_{\min}$ demonstrates strong sensitivity of P_{safe} to the chosen collapse-capacity threshold. Higher $\kappa_{\min}$ values rapidly reduce the range of acceptable post-mainshock damage, underscoring the importance of clearly defined safety criteria.
- A joint safety rule requiring all three EDPs (*PIDR*, *RIDR*, *DI*) to satisfy $P_{\text{safe}} \geq p_{\text{th}}$ provides a conservative basis for reoccupation decisions. The resulting $EDP_{crit}(\kappa_{\min})$ curves serve as practical thresholds: a building is safe only when its measured post-mainshock EDPs remain below all three corresponding critical values.

Overall, the study shows that, for the four-story steel special moment frame examined, the collapse safety index is highly sensitive to both the extent of initial damage and the characteristics of seismic demand, and that the selected safety threshold $\kappa_{\min}$ critically influences reoccupation classification. While the quantitative findings are specific to this case study, they illustrate how the proposed framework can be applied in practice and how different choices of $\kappa_{\min}$ affect safety tagging. The framework provides a structured and adaptable basis for post-earthquake safety evaluation, with potential for further development and application to other structural systems, performance levels, and intensity measures.

A particularly promising future extension is the integration of analytical predictions with post-earthquake field observations. Damage surveys documenting residual offsets, member yielding or local buckling, connection damage, story-mechanism development, and other structural or non-structural conditions could provide complementary building-specific evidence to verify the estimated damage state, refine the estimation of post-mainshock EDPs, and identify damage mechanisms not fully captured by the analytical model. Such information could be incorporated in future developments through Bayesian updating, whereby the probabilistic safety estimates obtained from the proposed framework would serve as prior probabilities and be updated using field observations to obtain posterior safety probabilities. Although this extension would further enhance the reliability of post-earthquake safety assessments, its implementation requires the development of probabilistic observation models and is therefore beyond the scope of the present study.

CRediT authorship contribution statement

Saeed Amiri: Conceptualization, Formal analysis, Investigation, Methodology, Writing – original draft. **Sanda Koboevic:** Conceptualization, Funding acquisition, Methodology, Supervision, Validation, Writing – review & editing.

Declaration of competing interest

The authors declare that they have no known competing financial interests or personal relationships that could have appeared to influence the work reported in this paper.

Acknowledgements

The financial support of the Natural Sciences and Engineering Research Council of Canada (NSERC) is gratefully acknowledged.

Data availability

Data will be made available on request.

References

[1] Rojah C. ATC-20-1 field manual: postearthquake safety evaluation of buildings, in Applied Technology Council: redwood City, CA, USA. 2005.
[2] Anagnostopoulos S, Moretti M. Post-earthquake emergency assessment of building damage, safety and usability—Part 1: technical issues. Soil Dynam Earthq Eng 2008;28(3):223–32.
[3] Carreño ML, Cardona OD, Barbat AH. Computational tool for post-earthquake evaluation of damage in buildings. Earthq Spectra 2010;26(1):63–86.
[4] Xue Y, Liu J, Yu H, Liu S. Seismicity characteristics of the 2011 M9.0 Tohoku earthquake near the East Coast of Honshu in Japan. Chin Sci Bull 2012;57(8):886–93.
[5] Guglielmi AV, Zotov OD, Zavyalov AD. The aftershock dynamics of the Sumatra-Andaman earthquake. Izvestiya Phys Solid Earth 2014;50(1):64–72.
[6] Amiri S, Garakaninezhad A, Bojórquez E. Normalized residual displacement spectra for post-mainshock assessment of structures subjected to aftershocks. Earthq Eng Eng Vib 2021;20(2):403–21.
[7] Amiri S, Koboevic S. Inelastic spectra under mainshock-multiple aftershock sequences. In: 3rd European conference on earthquake engineering & Seismology (3ECEES); 2022. Bucharest, Romania.
[8] Amiri S, Koboevic S. On the necessary number of aftershocks for seismic collapse risk assessment of buildings. In: 18th world conference on earthquake engineering (WCEE2024); 2024. Milan, Italy.
[9] Kazama M, Noda T. Damage statistics (summary of the 2011 off the Pacific Coast of Tohoku Earthquake damage). Soils Found 2012;52(5):780–92.
[10] Papazafeiropoulos G, Plevris V. Kahramanmaras-Gaziantep, Turkiye Mw 7.8 earthquake on February 6, 2023: preliminary report on strong ground motion and building response estimations. 2023. arXiv preprint arXiv:2302.13088.
[11] Gautam D, Chaulagain H. Structural performance and associated lessons to be learned from world earthquakes in Nepal after 25 April 2015 (MW 7.8) Gorkha earthquake. Eng Fail Anal 2016;68:222–43.
[12] Yetkin M, Dedeoğlu İÖ, Tunc G. Kahramanmaraş twin earthquakes: evaluation of ground motions and seismic performance of buildings for Elazığ, southeast of Türkiye. Soil Dynam Earthq Eng February 6, 2023;181:108678. 2024.
[13] Cetin KO, Ayhan BU, Cüceoğlu F, Yildirim S. Performance of Reyhanlı Dam during February 6, 2023 Kahramanmaraş-Türkiye earthquake sequence. Soil Dynam Earthq Eng 2025;194:109369.
[14] Araújo M, Macedo L, Marques M, Castro JM. Code-based record selection methods for seismic performance assessment of buildings. Earthq Eng Struct Dynam 2016;45(1):129–48.
[15] Amiri S, Soroushian A. A brief review on building structural analysis regulations in different seismic codes. Bull Earthq Eng 2017;20(1):1–24.
[16] Applied Technology Council (ATC). ATC-20 procedures for post-earthquake building safety evaluation procedures. 1995. Redwood City, CA.
[17] Federal Emergency Management Agency. Seismic performance assessment of buildings: methodology. 2012.
[18] Bazzurro P, Cornell CA, Menun C, Motahari M. Guidelines for seismic assessment of damaged buildings. In: 13th world conference on earthquake engineering. Canada; 2004. Vancouver.
[19] Luco N, Bazzurro P, Cornell CA. Dynamic versus static computation of the residual capacity of a mainshock-damaged building to withstand an aftershock. In: 13th world conference on earthquake engineering; 2004.
[20] Ruiz-García J, Aguilar JD. Aftershock seismic assessment taking into account postmainshock residual drifts. Earthq Eng Struct Dynam 2015;44(9):1391–407.
[21] Burton HV, Sharma M. Quantifying the reduction in collapse safety of main shock–damaged reinforced concrete frames with infills. Earthq Spectra 2017;33(1):25–44.
[22] Vamvatsikos D, Cornell CA. Incremental dynamic analysis. Earthq Eng Struct Dynam 2002;31(3):491–514.
[23] Burton HV, Sreekumar S, Sharma M, Sun H. Estimating aftershock collapse vulnerability using mainshock intensity, structural response and physical damage indicators. Struct Saf 2017;68:85–96.
[24] Zhang Y, Burton HV, Sun H, Shokrabadi M. A machine learning framework for assessing post-earthquake structural safety. Struct Saf 2018;72:1–16.
[25] Kalateh-Ahani M, Amiri S. A Park-Ang damage index-based framework for post-mainshock structural safety assessment. Structures 2021;33:820–9.

[26] Park Y-J, Ang AH-S. Mechanistic seismic damage model for reinforced concrete. J Struct Eng 1985;111(4):722–39.
[27] Galvis FA, Hulsey AM, Baker JW, Deierlein GG. Simulation-based methodology to identify damage indicators and safety thresholds for post-earthquake evaluation of structures. Earthq Eng Struct Dynam 2023;52(11):3455–76.
[28] Bianchini M, Diotallevi P, Baker J. Prediction of inelastic structural response using an average of spectral accelerations. In: 10th international conference on structural safety and reliability (ICOSSAR09); 2009. p. 2164–71.
[29] Bojórquez E, Iervolino I. Spectral shape proxies and nonlinear structural response. Soil Dynam Earthq Eng 2011;31(7):996–1008.
[30] De Biasio M, Grange S, Dufour F, Allain F, Petre-Lazar I. A simple and efficient intensity measure to account for nonlinear structural behavior. Earthq Spectra 2014;30(4):1403–26.
[31] Eads L, Miranda E, Lignos DG. Average spectral acceleration as an intensity measure for collapse risk assessment. Earthq Eng Struct Dynam 2015;44(12): 2057–73.
[32] Cosenza E, Manfredi G, Ramasco R. The use of damage functionals in earthquake engineering: a comparison between different methods. Earthq Eng Struct Dynam 1993;22(10):855–68.
[33] American Society of Civil Engineers. Seismic evaluation and retrofit of existing buildings. Reston, VA: ASCE/SEI 41-23; 2023.
[34] Fragiadakis M, Lagaros ND, Papadrakakis M. Performance-based multiobjective optimum design of steel structures considering life-cycle cost. Struct Multidiscip Optim 2006;32:1–11.
[35] Behnamfar F, Hosseini-Rad A, Habiby YM. A procedure for damage-based seismic design of moment frame structures. Bull Earthq Eng 2022;20(11):5877–904.
[36] Amiri S, Di Sarno L, Garakaninezhad A. On the aftershock polarity to assess residual displacement demands. Soil Dynam Earthq Eng 2021;150:106932.
[37] Kolmogorov A. Sulla determinazione empirica di una legge di distribuzione, vol. 4. Giorn Dell'inst Ital Degli Att; 1933. p. 89–91.
[38] Smirnoff N. Sur les écarts de la courbe de distribution empirique. Matematicheskii Sbornik 1939;48(1):3–26.
[39] Massey Jr FJ. The Kolmogorov-Smirnov test for goodness of fit. J Am Stat Assoc 1951;46(253):68–78.
[40] Dimitrova DS, Kaishev VK, Tan S. Computing the Kolmogorov-Smirnov distribution when the underlying CDF is purely discrete, mixed, or continuous. J Stat Software 2020;95:1–42.
[41] Stephens MA. EDF statistics for goodness of fit and some comparisons. J Am Stat Assoc 1974;69(347):730–7.
[42] Elkady A, Lignos DG. Modeling of the composite action in fully restrained beam-to-column connections: implications in the seismic design and collapse capacity of steel special moment frames. Earthq Eng Struct Dynam 2014;43(13):1935–54.
[43] Elkady A, Lignos DG. Effect of gravity framing on the overstrength and collapse capacity of steel frame buildings with perimeter special moment frames. Earthq Eng Struct Dynam 2015;44(8):1289–307.
[44] Elkady A, Lignos DG. Two-dimensional OpenSees numerical models for archetype steel buildings with special moment frames. Available from: https://github.com/amaelkady/OpenSEES_Models_SMF; 2019.
[45] Ibarra LF, Medina RA, Krawinkler H. Hysteretic models that incorporate strength and stiffness deterioration. Earthq Eng Struct Dynam 2005;34(12):1489–511.
[46] Mazzoni S, McKenna F, Scott MH, Fenves GL. OpenSees command language manual. Pacific Earthquake Engineering Research (PEER) Center; 2006. p. 137–58.
[47] Lignos DG, Hikino T, Matsuoka Y, Nakashima M. Collapse assessment of steel moment frames based on E-Defense full-scale shake table collapse tests. J Struct Eng 2013;139(1):120–32.
[48] Lignos D. Sidesway collapse of deteriorating structural systems under seismic excitations. Stanford University; 2008.
[49] Lignos DG, Krawinkler H. Deterioration modeling of steel components in support of collapse prediction of steel moment frames under earthquake loading. J Struct Eng 2011;137(11):1291–302.
[50] PEER/ATC. Modeling and acceptance criteria for seismic design and analysis of tall buildings. In: Prepared for Pacific earthquake engineering research Center (PEER) by Applied Technology Council (ATC): redwood City, CA; 2010.
[51] Gupta A. Seismic demands for performance evaluation of steel moment resisting frame structures. Stanford University; 1999.
[52] Silva V, Akkar S, Baker J, Bazzurro P, Castro JM, Crowley H, Dolsek M, Galasso C, Lagomarsino S, Monteiro R. Current challenges and future trends in analytical fragility and vulnerability modeling. Earthq Spectra 2019;35(4):1927–52.
[53] Bradley BA. A generalized conditional intensity measure approach and holistic ground-motion selection. Earthq Eng Struct Dynam 2010;39(12):1321–42.
[54] Baker JW. Conditional mean spectrum: tool for ground-motion selection. J Struct Eng 2011;137(3):322–31.
[55] Daneshvar P, Bouaanani N, Léger P. Application of conditional mean spectra for evaluation of a building's seismic response in Eastern Canada. Can J Civ Eng 2014; 41(8):769–73.
[56] Michaud D, Léger P. Ground motions selection and scaling for nonlinear dynamic analysis of structures located in Eastern North America. Can J Civ Eng 2014;41(3): 232–44.
[57] Goda K, Tesfamariam S. Multi-variate seismic demand modelling using copulas: application to non-ductile reinforced concrete frame in Victoria, Canada. Struct Saf 2015;56:39–51.
[58] Goda K, Tesfamariam S. Financial risk evaluation of non-ductile reinforced concrete buildings in eastern and western Canada. Int J Disaster Risk Reduct 2019; 33:94–107.
[59] Tesfamariam S, Goda K. Risk assessment of CLT-RC hybrid building: consideration of earthquake types and aftershocks for Vancouver, British Columbia. Soil Dynam Earthq Eng 2022;156:107240.
[60] Goda K, Atkinson GM. Seismic performance of wood-frame houses in south-western British Columbia. Earthq Eng Struct Dynam 2011;40(8):903–24.
[61] Pacific Earthquake Engineering Research Center. NGA-West2 ground motion database. Available from: https://ngawest2.berkeley.edu/.
[62] National Research Institute for Earth Science and Disaster Resilience. K-NET and KiK-net. Available from: http://www.kyoshin.bosai.go.jp/.
[63] Earthquake Research Institute. SK-net. Available from: http://www.sknet.eri.u-tokyo.ac.jp/.
[64] Goda K. Nonlinear response potential of mainshock–aftershock sequences from Japanese earthquakes. Bull Seismol Soc Am 2012;102(5):2139–56.
[65] Goda K, Taylor CA. Effects of aftershocks on peak ductility demand due to strong ground motion records from shallow crustal earthquakes. Earthq Eng Struct Dynam 2012;41(15):2311–30.
[66] Goda K, Wenzel F, De Risi R. Empirical assessment of non-linear seismic demand of mainshock–aftershock ground-motion sequences for Japanese earthquakes. Front Built Environ 2015;1:6.
[67] Jayaram N, Lin T, Baker JW. A computationally efficient ground-motion selection algorithm for matching a target response spectrum mean and variance. Earthq Spectra 2011;27(3):797–815.
[68] Raghunandan M, Liel AB, Luco N. Aftershock collapse vulnerability assessment of reinforced concrete frame structures. Earthq Eng Struct Dynam 2015;44(3): 419–39.
[69] Murthy DP, Xie M, Jiang R. Weibull models. John Wiley & Sons; 2004.
[70] Rinne H. The Weibull distribution: a handbook. CRC Press; 2008.
[71] Federal Emergency Management Agency. Quantification of building seismic performance factors. FEMA 2013;P695.